CFD INVESTIGATIONS OF A TRANSONIC SWEPT-WING LAMINAR FLOW CONTROL FLIGHT EXPERIMENT

A Thesis

by

TYLER PATRICK NEALE

Submitted to the Office of Graduate Studies of
Texas A&M University
in partial fulfillment of the requirements for the degree of

MASTER OF SCIENCE

May 2010

Major Subject: Aerospace Engineering

CFD INVESTIGATIONS OF A TRANSONIC SWEPT-WING LAMINAR FLOW CONTROL FLIGHT EXPERIMENT

A Thesis

by

TYLER PATRICK NEALE

Submitted to the Office of Graduate Studies of
Texas A&M University
in partial fulfillment of the requirements for the degree of

MASTER OF SCIENCE

Approved by:

Chair of Committee,	Helen Reed
Committee Members,	William Saric
	Hamn-Ching Chen
Head of Department,	Dimitris Lagoudas

May 2010

Major Subject: Aerospace Engineering

ABSTRACT

CFD Investigations of a Transonic Swept-Wing Laminar Flow Control

Flight Experiment. (May 2010)

Tyler Patrick Neale, B.S., Louisiana Tech University

Chair of Advisory Committee: Dr. Helen Reed

Laminar flow control has been studied for several decades in an effort to achieve higher efficiencies for aircraft. Successful implementation of laminar flow control technology on transport aircraft could significantly reduce drag and increase operating efficiency and range. However, the crossflow instability present on swept-wing boundary layers has been a chief hurdle in the design of laminar wings. The use of spanwise-periodic discrete roughness elements (DREs) applied near the leading edge of a swept-wing typical of a transport aircraft represents a promising technique able to control crossflow and delay transition to accomplish the goal of increased laminar flow.

Recently, the Flight Research Laboratory at Texas A&M University conducted an extensive flight test study using DREs on a swept-wing model at chord Reynolds numbers in the range of eight million. The results of this study indicated DREs were able to double the laminar flow on the model, pushing transition back to 60 percent chord. With the successful demonstration of DRE technology at these lower chord Reynolds numbers, the next logical step is to extend the technology to higher Reynolds numbers in the range of 15 to 20 million typical of smaller transport aircraft.

To conduct the flight tests at the higher Reynolds numbers, DREs will be placed on a wing glove attached to the aircraft wing. However, a feasibility study was necessary before initiating the flight-testing. First, a suitable aircraft able to achieve the Reynolds numbers and accommodate a wing glove was identified. Next, a full CFD analysis of the aircraft was performed to determine any adverse effects on the wing flow-field from the aircraft engines. This required an accurate CAD model of the selected aircraft. Proper modeling techniques were needed to represent the effects of the aircraft engine. Once sufficient

CFD results were obtained, they were used as guidance for the placement of the glove. The attainable chord Reynolds numbers based on the recommendations for the wing glove placement then determined if the selected aircraft was suitable for the flight-testing.

DEDICATION

This work is dedicated first to my parents, who have taught me the importance of hard-work and responsibility. Without their support and belief in me through the years, I would not have accomplished this goal of mine. I also dedicate this to my wife, Meredith, who has made many sacrifices to allow me to pursue this work and has always been by my side.

ACKNOWLEDGEMENTS

This work would not have been possible without the contributions from several different people. First, I must thank my advisor Dr. Reed. Since I first started working with her during my undergraduate years through the USRG program, she has provided me the guidance and motivation I needed to achieve this goal. Her efforts and consideration allowed me to attend Texas A&M for graduate school and gain countless valuable experiences. Without her support and sincere care, I do not believe I would have had such a successful and enriching experience at Texas A&M.

I also thank Dr. Saric, who served more as a co-advisor than just a thesis committee member. His expertise and experiences have given me great insight into the aerospace field. He taught me the importance of hard-work and perseverance that will make me a better engineer. I am also grateful for Dr. Chen for serving as my third committee member and Dr. White for always making time to answer any of my questions. My work would not have been possible without the assistance from Ms. Colleen Leatherman. She was always available to help in any way, and I cannot imagine the research group operating without her.

I would like to thank my fellow graduate students as well. Specifically, I thank Mike Belisle, who worked closely with me on my projects, Rick Rhodes, who provided valuable CFD expertise, Aaron Tucker, who gave me an excellent perspective on my career field, Matt Roberts, who will be continuing this research, and Celine Kluzek for her various contributions. I am also grateful for my friends Jan Tullos, who helped make my move to College Station an easy one, and Krystal Corbett, who was always available to give advice on graduate school.

Lastly, I must thank the SMART Scholarship Program for allowing me to pursue this degree and attain a position with the U.S. Air Force. It has served as an excellent funding source and has given me the opportunity to fulfill my childhood dream of working for the Air Force. Specifically, I thank Mr. Tom Best for selecting me as a recipient of the award and my cohort administrator Ms. Stephanie Yingling for assisting me with any questions or issues regarding my SMART scholarship.

NOMENCLATURE

A	Area
Cp	Pressure coefficient
F	Fahrenheit
L/D	Lift over drag ratio
lbm	Pound (mass)
$\dot{m}$	Mass flow rate
M_w	Molecular weight
p	Pressure
psfa	Pounds per square foot (absolute)
R	Rankine
$\overline{R}$	Gas constant
S	Seconds
T	Temperature
x/c	Percent chord
α	Angle of attack
β	Side-slip angle
ρ	Density

TABLE OF CONTENTS

Page

LIST OF FIGURES

Page

LIST OF TABLES

1. INTRODUCTION

The research and work described in this thesis pertains to the development of technology for achieving laminar flow on transport aircraft. The difficulty of maintaining laminar flow on this type of aircraft is exacerbated by the wing sweep, which has several associated mechanisms that can lead to transition. Understanding each of these mechanisms and how they can be controlled is essential for developing laminar flow technology.

A promising technology known as periodic discrete roughness elements (DREs) has shown great potential for achieving laminar flow on swept wings. DREs have been demonstrated in wind tunnels and low Reynolds number flight tests, and in order to progress in the maturation process, the next step is to demonstrate the technology at higher Reynolds numbers. To do this, the Flight Research Laboratory at Texas A&M University is proposing to conduct an extensive flight test program using a business jet-type aircraft as the test bed. A wing glove that will accommodate the DREs will be mounted on the aircraft's wing for the flight testing. The extent of laminar flow achieved on the wing glove will indicate the effectiveness of DREs at higher Reynolds numbers. However, before performing the actual flight tests, a feasibility study is needed to ensure the selected aircraft is suitable for the flights. This study includes the selection of a candidate aircraft, the creation of a CAD model of the particular aircraft, and a full CFD flow-field analysis using the model. The work presented below details the processes and methods for determining the feasibility of a particularly selected aircraft for the laminar flow control study.

1.1 Background in Laminar Flow Control

The study of laminar flow can be traced back several decades to the early aeronautical pioneers. Benefits such as longer range and higher efficiency have driven the research towards creating laminar flow aircraft. Recently, the push for lower emissions and the volatility of fuel prices have helped emphasize the importance of this technology. Both of these factors equate to reducing fuel burn during flight.

This thesis follows the style of the *AIAA Journal.*

Airline data from the Bureau of Transportation Statistics [1] show the importance of fuel burn for the airline industry. As detailed in a December 2009 report, the cost of fuel accounts for an average of nearly 24 percent of the total operating costs for the seven major United States network carriers. This figure increases to nearly 32 percent for low-cost airlines. These percentages have increased from their 2004 levels of 17.8 and 20.5 percent for the major carriers and low-cost airlines, respectively. Fig. 1 shows the increase in fuel cost in dollars per gallon for airlines over the past decade. While the figures have decreased from their highs in 2008, there is still a troubling upward trend for the prices. With fuel costs amounting to about one-fourth of the operating cost for the major airlines, laminar flow technology could significantly reduce operating costs. This would not only help the airline industry but also the consumer.

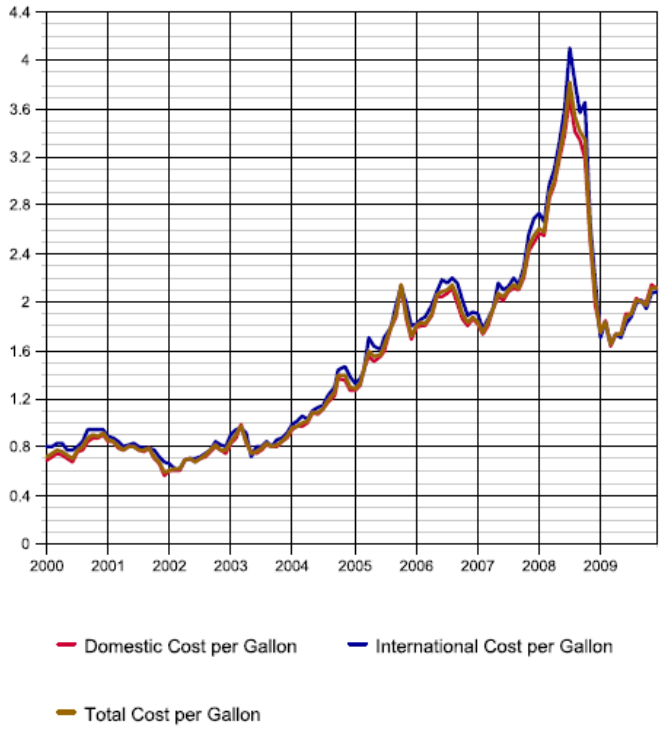

Fig. 1 Cost of fuel per gallon over the past decade [1].

Green [2] explains in detail how laminar flow can help significantly reduce the amount of fuel burned during a flight. It is well understood that reducing the profile drag of an aircraft will improve its L/D and

thus its efficiency. Laminar flow represents a very promising method for improving L/D by reducing the drag associated with the aircraft's wing. The reduction in drag can be attributed to less shear stress at the wall, also known as skin friction. The shear stress along the surface of a wing is proportional to the streamwise velocity gradient. Since a turbulent boundary layer has a much fuller velocity profile and, thus, greater velocity gradient than a laminar boundary layer, it produces higher skin friction at the wall. Therefore, aircraft with laminar wings produce less skin friction which allows them to be more fuel efficient.

1.2 Transition Mechanisms

The transition to turbulence for aircraft can be a complicated and daunting process to study. However, work over the past several decades has brought a greater understanding of this field. Transition is considered to start with a process known as receptivity, as discussed in Reed et al. [3]. This involves disturbances from the free-stream flow entering the boundary layer and modifying the basic state. These disturbances then grow within the boundary layer until they become amplified enough to trigger a transition to turbulence. A few key mechanisms can be attributed to this transition to turbulence. Reed et al. [3] outlines these four basic instability mechanisms: attachment-line contamination, Görtler vortices, Tollmien-Schlichting waves, and crossflow.

Attachment-line contamination originates from the sweep angle and leading-edge radius of the wing. This mechanism can typically be eliminated by limiting the leading-edge nose radius for certain sweep angles. A second mechanism involves the instability produced from concave curvature on the wing surface.

Concave wall curvature produces streamwise, counter-rotating vortices known as Görtler vortices. Again, this instability can be controlled by avoiding concave curvature or taking special care when designing the airfoil.

The third mechanism, which typically exists in low-disturbance flow-fields such as flight, is a streamwise instability triggered by Tollmien-Schlichting (T-S) waves. This viscous instability occurs in

regions of adverse pressure distributions. However, T-S waves can be controlled with a favorable pressure gradient present for the majority of the wing chord.

The fourth primary transition mechanism, the crossflow instability, represents the greatest challenge to laminar flow on swept-wings, and therefore it is of most interest on modern, swept-wing transport aircraft. Crossflow occurs in three-dimensional boundary layers with strong favorable pressure gradients. It gives rise to an instability present on aircraft with any significant wing sweep. Saric et al. [4] give an excellent overview of the crossflow instability. Outside the boundary layer in the inviscid region, the wing sweep and pressure gradient cause the streamlines to become curved. Within the boundary layer, the velocity reduces due to the no-slip condition. However, the pressure inside the boundary layer as is constant, equal to the gradient at the edge of the inviscid region. This produces an imbalance between the pressure gradient and the centripetal acceleration and leads to a secondary boundary layer flow called crossflow that is transverse to the inviscid streamlines. Since the crossflow does not exist outside the boundary layer, it must vanish at the boundary layer edge. However, the crossflow also disappears at the wall due to no-slip, thus producing an inflection point. Fig. 2 shows a typical swept-wing boundary layer profile with a crossflow instability. The presence of an inflection point provides a source for an instability of co-rotating vortices with axes nearly aligned to the inviscid streamlines.

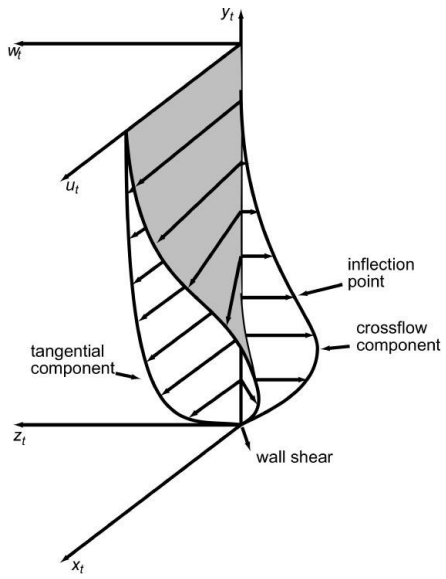

Fig. 2 Boundary layer profile for swept-wings [4].

Crossflow disturbances exist as both stationary and traveling waves, though transition is typically triggered by one before the other. Traveling waves are characteristic of high-turbulence environments while stationary waves dominate in low-turbulence environments [5]. For stationary waves, two weak velocity disturbances exist, with one tangent to the surface (v') and the other parallel to the leading edge (w'). The v' and w' waves convect high-momentum fluid toward the wall and low-momentum fluid upward, away from the wall. These displacements then lead to a streamwise disturbance that quickly amplifies and eventually leads to large disturbances imposed on the basic state. Once this disturbance becomes too large, the streamwise velocity begins to rollover and leads to a breakdown in the boundary layer and eventually transition to turbulence.

1.3 Laminar Flow Control Techniques

The challenge in achieving laminar flow for an aircraft comes from attempting to control the previously described transition mechanisms associated with transport aircraft. Saric et al. [6] explain the most appropriate method for laminar flow control implementation is to incorporate the control directly into the conceptual design phase, rather than retro-fitting it onto an existing platform. Multiple approaches can

be taken in implementing laminar flow control. Natural laminar flow (NLF) control passively stabilizes the flow with a favorable pressure gradient along the majority of the wing. This assists in delaying transition as far aft along a two-dimensional airfoil as possible but will eventually fail with increased wing sweep or Reynolds number. This fact significantly reduces the usefulness of NLF control, as most transport aircraft have an appreciable wing sweep that would render the technique useless. With the higher wing sweep angles, suction can be applied at the leading edge of an NLF airfoil to achieve laminar flow. The leading-edge suction helps to minimize the crossflow instability associated with swept-wing aircraft. Wagner et al. [7] give further analysis and results for leading-edge suction systems. This method is known as Hybrid Laminar Flow Control (HLFC). Both NLF and HLFC methods attempt to prevent crossflow and control T-S waves. Though HLFC is applicable to swept-wing transport aircraft, the possible complications and complexity of the mechanical system associated with suction make this technique undesirable. Green [2] provides further information for these laminar flow technologies.

Considering the disadvantages of NLF and HLFC, Saric et al. [8] proposed a third laminar flow control technique for swept-wing aircraft termed Swept-Wing Laminar Flow Control (SWLFC). This method aims to eliminate any streamwise instability while modifying the meanflow in attempt to control any growth of crossflow waves. During the design phase of the airfoil, leading-edge contamination can be eliminated through effective design of the leading-edge radius, as previously discussed. Similarly, Görtler vortices are avoided through the avoidance of concave wall surfaces. Troublesome T-S waves can be eliminated by developing an airfoil with a favorable pressure gradient and minimized pressure recovery region. This leaves crossflow as the only transition mechanism left to be considered.

To control the crossflow instability, it should be recognized that in low-disturbance environments such as flight, stationary crossflow waves are dominant. Radeztsky et al. [9] demonstrated in wind tunnel experiments that micro-meter-sized roughness elements can be used to influence transition caused by crossflow. Three-dimensional roughness elements act as a source for streamwise vorticity, which can influence the amplitude of the stationary crossflow wave. Saric et al. [10] extended upon this work by successfully demonstrating through wind tunnel experiments that DREs can effectively delay transition on a swept-wing beyond the pressure minimum. Specific crossflow wavelengths can be excited by the

spacing of the DREs and reach their growth peak before causing transition. The basic state is distorted by this forced wave, and this has a stabilizing effect on the originally most unstable crossflow wave.

The use of DREs capitalizes on two important findings by Reibert et al. [11]. The unstable crossflow waves only appear at integer multiples of the primary disturbance wavenumber, and no subharmonic disturbances become destabilized by the DRE spacing. Using these findings, DREs can be tailored for different flow environments. As outlined in Saric et al. [8], the most unstable stationary crossflow wavelength must first be identified, typically through linear stability theory. Next, a subcritical wavelength is chosen that will be forced by the DRE spacing. The shorter, forced wavelength will grow strongly initially and then decay quickly, modifying the basic state and preventing the most unstable wave, which has a larger wavelength, from growing. Therefore, effective DRE spacing can successfully delay transition by inhibiting the growth of the most unstable crossflow wave.

While the wind tunnel experiments demonstrated successful implementation of DREs on swept-wing models, the results cannot necessarily be applied to the flight environment. As mentioned previously, stationary crossflow waves are responsible for transition in a flight environment. Though wind tunnels can be designed to have minimal disturbances, known as quiet wind tunnels, they cannot completely replicate the low-disturbance conditions associated with flight. Therefore, in order for DRE technology to be successfully validated for use on aircraft, it must first be demonstrated through experiments in a flight environment.

1.4 Predecessor to Current Work

To demonstrate DRE technology in a flight environment, the Flight Research Laboratory at Texas A&M initiated an extensive flight test with a Cessna O-2A aircraft. For the flight tests, a test article was created, called the Swept-Wing In Flight Testing (SWIFT) model, that was mounted vertically below the port wing on a wing pylon. The flight tests were conducted to achieve chord Reynolds numbers in the range of 6.5 and 7.5 million, which represented a modest range for validating the technology in flight. This represented a logical step in the maturation of the DRE technology. Carpenter et al. [12] explain in great detail the entire project. The aircraft and the SWIFT model can be seen below in Fig. 3.

Fig. 3 O-2A with SWIFT model vertically mounted on port wing.

In order to test the effectiveness of different DRE configurations, the SWIFT model contained an interchangeable leading-edge insert. With this, baseline tests could be run with different leading edges without DREs. When tests requiring DREs along the leading-edge were needed, different inserts containing DREs could be placed on the model. The chord of the SWIFT was 54 in. and the leading-edge sweep was 30 degrees.

In order to achieve the desired Reynolds numbers, high-speed descents were conducted to gather flight data. Once the test conditions were reached, infrared (IR) thermography was used to identify regions that were laminar or turbulent. Gartenberg et al. [13] discuss the history and application of IR thermography used for aerodynamic research. The technology is very attractive for studies such as this since it provides a global view of the region of interest. Turbulent flow has a much higher heat transfer rate than laminar flow; thus, turbulent regions on the SWIFT would appear hotter on the IR flight image during the high-speed descents [14]. A certain temperature differential between the surrounding atmosphere and the

SWIFT surface is required in order to allow enough heat transfer to distinguish between turbulent or laminar regions. Conveniently, the high-speed descent required to achieve the Reynolds number assisted with the temperature differential requirement. By remaining at a higher altitude, typically 10,500 ft., for a period of about 30 minutes, the SWIFT model was cold-soaked. As the plane descended during its dive, it entered warmer atmosphere, thus providing sufficient heat transfer for the IR thermography.

During the high-speed descent, Cp data was recorded by two rows of pressure ports on the SWIFT model. While the Cp data was used in a boundary-layer code to generate boundary-layer profiles, it was also used to compare results to an extensive CFD study of the SWIFT. Rhodes et al. [15] explain in detail the CFD effort that accompanied the flight testing. Serving as a companion to the flight testing, the CFD study involved both the SWIFT model and an extensive portion of the O-2 aircraft.

Once satisfactory agreement between the Cp data from flight and the computational effort was achieved, the CFD results could be used to provide boundary-layer profiles and stability analyses. The O-2 CFD model was constructed such that boundary layer data could be extracted from the flow-field solution via a custom User-Defined Function (UDF). The data extracted by the UDF was then used in a robust stability analysis code. This code calculated the most destabilizing wave-number and its respective chordwise neutral point, which is where the disturbance initially develops. Recommendations on the optimal placement of the DREs on the SWIFT model were made based on these stability results. This not only saved flight time but also made the flights more productive.

The computational effort associated with the SWIFT flight testing was extremely successful. After numerous iterations between the flight testing and the CFD modeling, excellent agreement was accomplished between the two efforts, shown in Fig. 4. Many valuable lessons were also gained through the testing; for example, proper placement of a five-hole data probe was found through a CFD investigation. For the CFD testing, correct boundary conditions were derived from flight data by accounting for streamline deflection caused by the O-2 fuselage and the SWIFT model. These and other lessons allowed such good agreement between the two efforts and help create a foundation for future CFD studies.

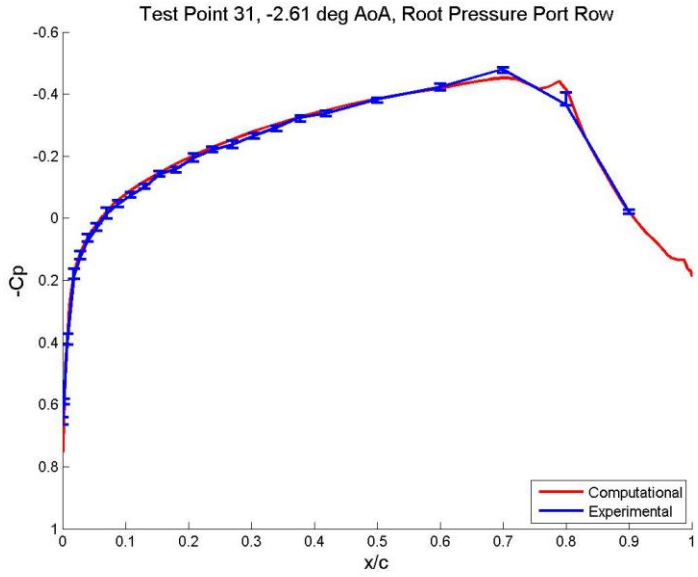

Fig. 4 Comparison of flight and computational results for SWIFT [15].

1.5 Objectives

With the successful demonstration of DRE technology to promote laminar flow on swept-wings at chord Reynolds numbers around eight million, the next logical step was to extend this effort to higher Reynolds numbers. A chord Reynolds number in the range of 15 to 20 million is typical of a small transport aircraft, such as a business jet, and this range represented an excellent step towards eventually proving the technology on large transport aircraft with chord Reynolds numbers around 30 million. A business jet platform was expected to have the required performance and design characteristics needed to achieve the chord Reynolds number between 15 and 20 million. The desired flight conditions and aircraft characteristics are detailed in Table 1. As opposed to the SWIFT model on the O-2, this experiment would utilize a wing glove mounted over the aircraft's wing. The wing glove would be designed to be subcritical to T-S instabilities by having an accelerated Cp for the majority of the chord. With the elimination of T-S waves, only the crossflow instability should be present in the boundary layer, thus allowing DREs to be utilized to achieve laminar flow.

Table 1 Target parameter values for LFC experiment.

Parameter	Value
Chord Reynolds No.	15-20 million
Mach No.	0.75
Altitude	40,000 ft.
Wing Sweep	30°

In order to initiate an LFC study at the desired chord Reynolds numbers, three different aspects needed to be considered. First, a suitable aircraft that could be used for the flight testing needed to exist and be available. Second, an extensive CFD study would need to be initiated in order to determine any flow-field interference from the aircraft engines and any streamline deflection due to the fuselage that could adversely affect the experiment. Atypical pressure distributions that are not relatively spanwise-constant on the wing glove could prevent any laminar flow even with the use of DREs. The streamline deflection could potentially change the α or β the wing glove experiences. The results of the CFD study would provide recommendations for effective wing glove placement on the selected aircraft. Finally, these results would aid in the design of a suitable airfoil with an appropriate pressure distribution for using DREs to control crossflow instabilities. This study concerns the candidate aircraft selection and CFD study tasks.

2. AIRCRAFT SELECTION

2.1 Selection Process

To extend upon success of the SWIFT flight experiments at eight million chord Reynolds number, a suitable aircraft was needed to achieve the desired 15 to 20 million chord Reynolds number. Without an aircraft capable of this specification, the entire project would be ended. The feasibility of a test bed aircraft represented the first step in the project's conceptual design process. While this initial requirement may seem trivial, several factors needed to be considered, making the process much more in-depth.

To start, the primary factors influencing the chord Reynolds number include the wing chord length, cruise speed, and cruise altitude. Furthermore, to help satisfy requirements for creating a laminar swept wing, a wing sweep of 30 degrees was targeted. With these factors in mind, a business jet platform became very attractive. These types of aircraft would be able to achieve the required speed and have an appropriate size. Wing sweep angles for these aircraft were typically close to 30 degrees as well. Propeller-powered aircraft were not considered, as they would be unable to achieve the required speed. Similarly, supersonic aircraft were also disregarded since they would have excessively high Reynolds numbers.

Over 70 different business jets were initially examined as potential candidates for the project. The complete list of the aircraft can be found in Appendix A. To gather information about each of the aircraft, the online database *Jane's Aircraft Upgrades* [16] was utilized. This source provided design, performance, and historical information on the aircraft, as well as often providing supplementary pictures. Once the list of candidate aircraft was completed, each aircraft was given a grade according to the following criteria: location of the engine nacelles, cruise speed, cruise altitude, and wing sweep angle. The highest scores were given to aircraft that had fuselage-mounted engines, a cruise speed of Mach 0.8, a cruise altitude of 40,000 ft., and a wing sweep angle of 30 degrees. The significance of the fuselage-mounted wings exists because engines mounted beneath the wing would have an adverse effect on the flow-field over the wing. Any aircraft that did not satisfy all four of these basic criteria was eliminated from the candidate list. This significantly reduced the number of potential aircraft.

After this first reduction, chord lengths and obtrusive control surfaces were examined on the remaining candidate aircraft. Small chord lengths would prevent the aircraft from achieving the desired chord Reynolds number, while obtrusive control surfaces could interfere with the wing glove mounting. Again, this further reduced the number of candidate aircraft for the project.

Finally, the availability of extant aircraft for the flight testing was examined. The project would require an estimated six months for the flight testing and sole-use of the selected aircraft during this testing time-frame. Otherwise, removing and reapplying the wing glove and instrumentation could prove difficult and affect the results. Permission would also be needed to modify the aircraft by mounting a wing glove and installing necessary equipment. Therefore, aircraft owned by flight testing agencies remained the only ones suitable for the project, and those available through leasing agencies were eliminated.

2.2 Final Candidate Aircraft

Considering all of the criteria and requirements previously stated, the final candidate aircraft consisted of the Gulfstream II and III and the Sabreliner 80. These three similar aircraft met all of the performance specifications, had fuselage-mounted engines, contained limited obtrusive control surfaces, and were available through agencies that would allow modification and extended, sole-use flight testing. Table 2 lists various specifications for the three selected aircraft.

As the smallest of the three, the S-80 has as 28.5 degree wing sweep and a 44 ft. 8 in. wing span. It uses two General Electric CF700-2D-2 turbofan engines as its power plant. Since it is the smallest aircraft selected, it would potentially need to fly at lower altitudes than the Gulfstream jets in order to achieve the desired chord Reynolds number. Another option would be to place the wing glove further inboard to gain a larger chord; unfortunately, the flow-field in this region could be negatively affected by the closer proximity of the engine. However, it was available through Flight Test Associates based in Mojave, CA, making it an attractive choice for the flight testing.

The first production G-II first flew in October 1966. The standard version has a wing span of 68 ft. 10 in., with a gross wing area of 809.6 ft^2. The engines used are two Rolls-Royce Spey Mk 511-8 turbofan engines. Similar to the G-II, the G-III was essentially an upgrade of the G-II aircraft. Slightly larger, the

G-III had a 77 ft. 10 in. wing span and an increased gross wing area of 934.6 ft^2. It used the same power plants as the G-II. The G-III's first flight was made in December 1979.

Table 2 Selected aircraft specifications.

Aircraft	Wing Span (ft.)	Wing Sweep	Max Cruise Speed	Max Altitude (ft.)
S-80	44.5	28.5°	M 0.8	45,000
G-II	68.83	25° (c/4)	M 0.85	43,000
G-III	77.83	27.67° (c/4)	M 0.85	45,000

Besides the standard G-II, two separate versions were also developed. The G-II/B is a modified G-II with a G-III wing. With the longer wing span, the G-II/B had a longer range and higher fuel efficiency. Another upgraded version, termed the G-II/SP, has Aviation Partners blended winglets installed on the wing tips. The winglets increase the wing span to 73 ft., which gives the G-II/SP a longer range and improved performance and efficiency. Conveniently, the upgrade also includes the removal of wing fences, which provided a more unobstructed area to mount a test article.

2.3 Selection of the G-II

Through discussions with NASA-DFRC and FTA during the initial stages of the project, the selection of the aircraft converged on the NASA G-II/SP with tail number N949NA and the Aviation Partners winglets. Since the G-II is larger than the S-80, the desired chord Reynolds number would be more easily obtained. This made the G-II a more attractive aircraft for the testing. While the G-III had a larger chord, it was unavailable through NASA during the planned flight testing time period. These factors led to the initial selection of the G-II/SP (N949NA), which was expected to be available for the flight testing for the required six months.

With this selection, a full CFD analysis of the aircraft was initiated. While the results from the CFD tests would be specific to the G-II, any conclusions reach could be extended to the G-III and S-80 in case plans for the test-bed aircraft changed. In fact, since the G-III and G-II both use the same power plant,

results from the G-II study could be considered very applicable to the G-III. This fact made the CFD analysis a vital role in the development of the wing glove for flight testing. The selected G-II can be seen in Fig. 5 below.

Fig. 5 The NASA G-II/SP (N949NA) on a tarmac in El Paso, TX.

3. DEVELOPMENT OF CAD MODEL

With a preliminary aircraft selected for the flight testing, a full CFD study of the flow-field represented the next task in the project. This was needed in order to determine any effects the fuselage-mounted engines may have on the wing flow-field. With the nacelles impinging slightly over the G-II wing near the root, their effects could alter the pressure distribution on the wing. This could potentially prevent any LFC testing from taking place in the affected region. These facts necessitate the extensive CFD study discussed in the proceeding sections.

3.1 Scanning of the G-II/SP

The first step in the CFD process is obtaining a CAD model of the aircraft of interest. Often times, these models are available through the manufacturer. However older aircraft often do not have reliable CAD models. Even if a model had been generated, the manufacturer can be reluctant to release them due to proprietary reasons. When models are not available, a viable solution is performing a laser scan of the aircraft and creating a CAD model from the data.

Unfortunately, a readily-available model of the G-II was not available. Being an older aircraft built in the late 1960s, CAD models were not made during the aircraft's development. Therefore, in order to obtain an accurate three-dimensional computer model of the G-II, Direct Dimensions, Inc. (DDI) from Owen Mills, MD was contracted to perform a detailed laser scan of the aircraft and subsequently create a three-dimensional CAD model. This model would, in turn, be implemented into a CFD solver to calculate the aircraft flow-field. Scanning took place in early December 2008 over the course of two days in El Paso, TX where this particular G-II was residing.

To scan the aircraft, DDI used a Surphaser 25 HSX medium range laser scanner, which delivered single-point accuracies of about 0.01 in. The G-II was placed on jacks for the duration of the scan and was housed inside a hangar. To reduce both scanning time and computational time of the model, only half of the aircraft was scanned, treating a vertical plane through the center of the aircraft as a plane of symmetry. The empennage of the G-II was also ignored during the scanning process since it was determined to have

no effect on the wing flow-field. Again, this minimized the cost of the scan and reduced computational requirements.

The laser scanning process involves passing a laser line over the surface of the object, recording three-dimensional information. A camera sensor mounted within the laser scanner records the data as dense three-dimensional points in space. The process is detailed in an educational feature on DDI's website [17]. For the G-II, approximately 2.8 billion total points were gathered during 41 scans to create the three-dimensional model.

With the scanned data of the G-II, DDI then developed a usable solid CAD model of the aircraft with the software program Imageware. The initial model was received on January 23, 2009. Since one of the primary goals of the CFD study was to determine the effects of the engine on the wing's flow-field, multiple variations of the G-II model were created. The first contained a flow-through nacelle that had no faces at the inlet or outlet of the engine, allowing the air to flow freely through the nacelle. While this model would capture the aerodynamic effects of the nacelle inlet, it would not be able to simulate any effects of the turbofan. It also would not represent an accurate flow rate through the nacelle. The second model, called the closed nacelle model, contained solid faces at the inlet and outlet of the engine, preventing any flow from passing through. These faces could later be assigned boundary conditions in order to simulate the effects of an operating engine. The final model variation did not contain any of the nacelle structure on the aircraft. This no-nacelle model was created to serve as a baseline so that results obtained with the model could be compared to the models containing the nacelle. This would allow conclusions to be made regarding the influence of the engine on the flow-field. The closed nacelle model and no-nacelle model were the two primary models used for the computations. Views of the generic CAD model are seen in Fig. 6 and Fig. 7.

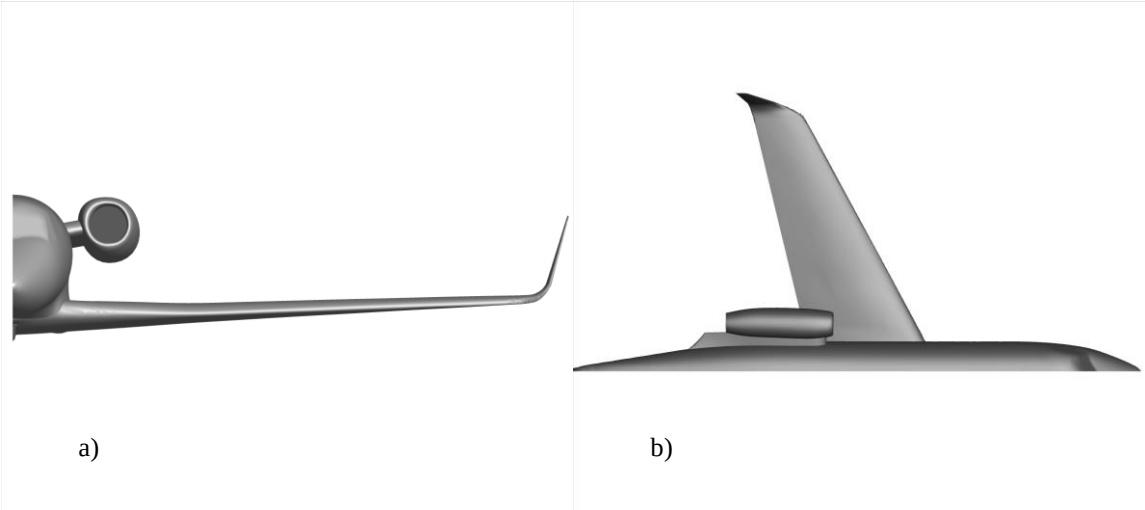

a) b)

Fig. 6 CAD model created from laser scan. a) Front view. b) Top view.

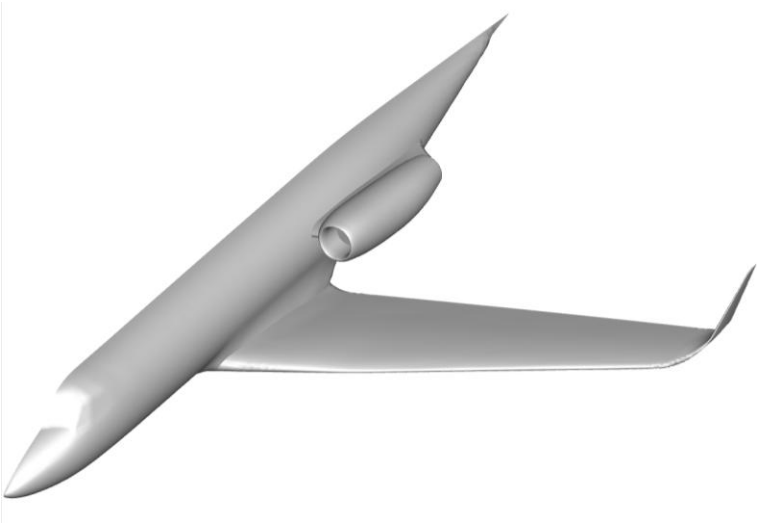

Fig. 7 Isometric view of G-II/SP CAD model.

3.2 Complications with Initial Model

After receipt of the initial model, a rudimentary CFD analysis was performed to obtain preliminary flow-field results. A more in-depth description of the CFD setup will be discussed in the next section. The conditions used for this analysis were a free-stream velocity of Mach 0.8, a free-stream pressure of 500

psfa, and a static temperature of -59.8° F. These values were simply rough figures for this preliminary test only.

After obtaining suitable convergence on all three models, the CFD results were analyzed. The Cp at different spanwise locations was taken from the results and plotted. Upon inspection, unexpected behavior of the pressure distribution appeared immediately aft of the leading edge. This irregularity was present on all three models at about ten percent chord, indicating it was unrelated to the presence of the engine and possibly due to surface geometry.

As seen in Fig. 8, waviness in the Cp plots occurred around ten percent chord at different wing stations. This type of pressure distribution for an airfoil was not considered to be realistic; therefore, it was determined that the waviness was caused by the geometric model created from the scan data. DDI was notified of the issue and a full investigation into resolving the modeling of the wing was initiated.

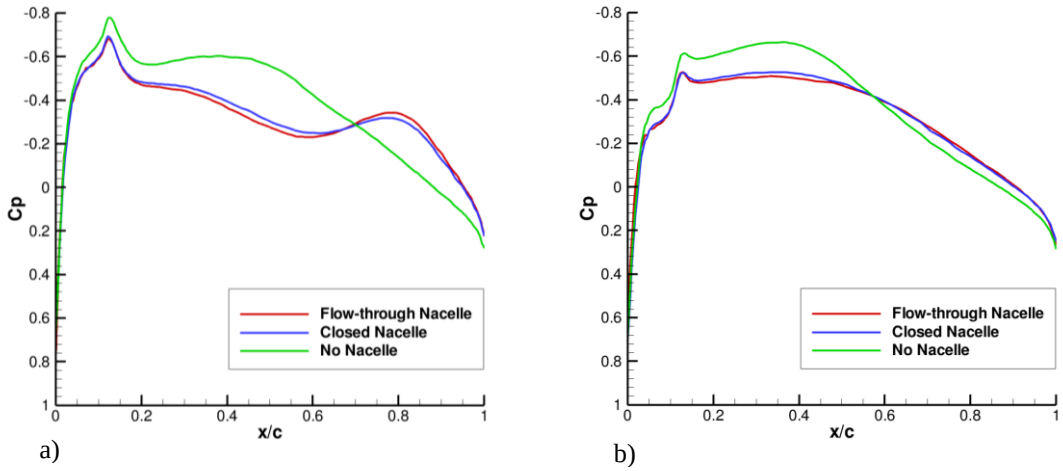

Fig. 8 Cp comparison between different models. a) 25% span. b) 45% span.

After discussions, DDI suggested the problem may be occurring at an interface between two different lines that defined the airfoil. When creating the wing model, DDI used multiple airfoil profiles along the span to create the wing. This entailed creating lofts between each two-dimensional airfoil profile. To create each particular airfoil profile, DDI initially used three different line segments: a leading edge, a

suction side, and a pressure side. The three lines were then stitched together at their interfaces, creating the airfoil profile. After noticing the waviness of the pressure distribution was occurring at the interface between the leading edge and suction side, it was determined that discontinuities in the surface geometry were causing the irregularities.

In order to confirm the source of the waviness, several two-dimensional CFD studies were performed on airfoil sections provided by DDI of the wing model. These were simply streamwise slices of the three-dimensional wing. Three different airfoil profiles were provided by DDI, each employing a different modeling technique. The first airfoil was created using a tangent-continuous boundary condition at the interface between the leading edge and suction edge. This technique only ensured that the tangent of the wing surface remained constant across the interface; any higher derivatives of the lines were not necessarily constant. A second airfoil was created using a curvature-continuous boundary condition at the interface. This went one step further than the previous technique, as it ensured that the curvature of the lines remained constant across the interface. Finally, the third model provided used a single spline to model the airfoil. Since this created one single line for the airfoil, all derivatives of the line remained constant throughout. All three airfoil models remained within the originally specified geometrical tolerances.

A structured grid, shown in Fig. 9, was created around each two-dimensional airfoil. The parabolic computational domain extended 20 chord lengths in front of the airfoil and 40 chord lengths behind to prevent any edge effects from the boundaries from affecting the solution. These computational meshes were then used to compute the flow-field. The conditions used for these tests were the target conditions of Mach 0.75 at an altitude of 40,000 ft according to U.S. Standard Atmosphere 1976 [18]. Since these CFD cases required a relatively small amount of resources, they were quickly completed.

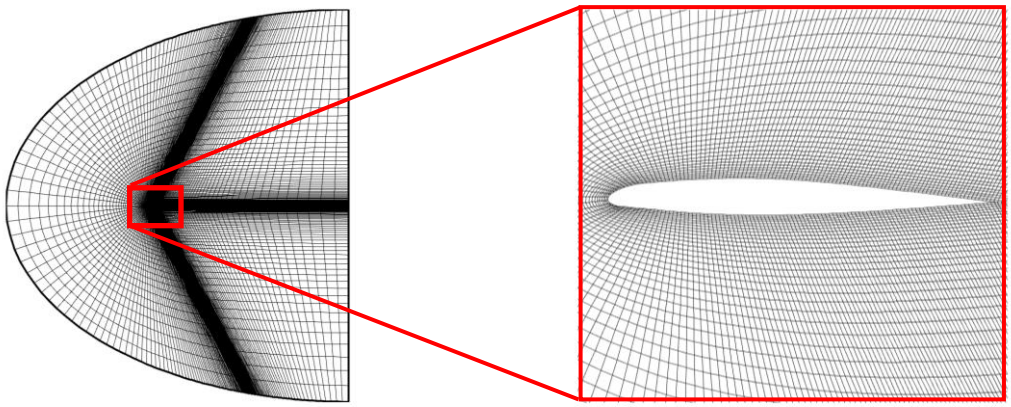

a) b)

Fig. 9 Computational mesh used for airfoil study. a) Full flow-field mesh. b) Close-up of airfoil surface mesh.

Fig. 10 shows the Cp plots for the three different airfoils. The first airfoil version produced a Cp plot very similar to the plots of the full aircraft model. This was expected, as both models used the same technique for creating the airfoil profiles. The second airfoil version also produced similar results to the three-dimensional model. Waviness still occurred around ten percent chord. However, the third airfoil version, which used a spline, produced a very smooth and more realistic Cp plot. The waviness previously at ten percent chord was no longer present. These results led to the conclusion that the irregular pressure distribution near the leading edge was due to discontinuities at the interface between the leading edge and suction edge of the model. Since using a spline to model the scanned data did not involve any interface near the leading edge, the airfoil profile remained continuous throughout its length. Therefore, this became the desired technique for creating the wing model of the G-II. The iterative process taken to converge on a suitable modeling technique for the aircraft wing served as a valuable learning experience both for Texas A&M and DDI.

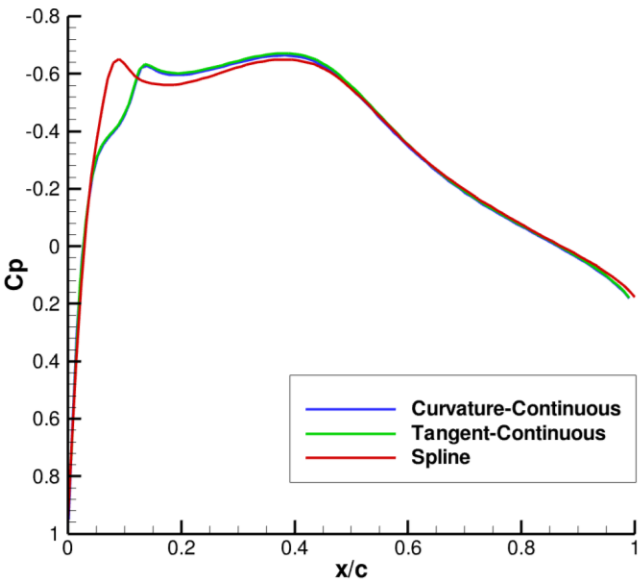

Fig. 10 Cp plots for the three different airfoil models.

Before implementing the new technique for creating the G-II wing into the full aircraft, the spline model was used incrementally to create a new aircraft model. First, the Cp at multiple wing stations spanning from near the root to near the winglet of the wing were examined. All wing stations produced good pressure distributions, allowing the spline airfoil sections to be used for a three-dimensional wing section.

Once a wing section was created from the spline wing stations, a three-dimensional CFD case was created to test the quality of the new model. Again, positive results were obtained from this computational study. By establishing the confidence in using the spline technique, DDI constructed the improved full G-II wing. A high-fidelity mesh was created for this wing model, and the flow-field solution was computed. The results of this test showed the wing was ready to be stitched to the fuselage, completing the modeling process.

The primary concern with using the spline technique to create the wing geometry was whether or not the actual surface of the aircraft had discontinuities. If this was the case, then the Cp results would be

indicative of the aircraft wing. While the as-designed geometry could be designed to be completely smooth, the physical aircraft may have been built with discontinuities on the surface. Therefore, the spline model could be viewed as an ideal representation of the wing. Without the actual raw scan data of the wing surface available, it would not be known whether the discontinuities actually exist. Access to flight data Cp could conceivable resolve all uncertainties about the surface geometry. If flight Cp plots had the irregularities at the leading edge, then the original wing modeling technique could in fact be accurate. However, for the current work, the ideal representation utilizing a spline fit was considered the best option for modeling the aircraft wing. The CAD model created using splines for the wing still remained within the tolerances specified and still provided a highly accurate representation of the wing.

4. CREATING THE COMPUTATIONAL MESH

4.1 Previous Experiences with Aircraft CFD

Previously, extensive CFD work had been performed on a full aircraft model of the O-2 operated by Texas A&M's Flight Research Laboratory. Many techniques and lessons were discovered through this work, which were then extended to the G-II project. The CFD studies performed on the O-2 helped establish a foundation for future studies of aircraft.

For the work on the O-2, a full aircraft CAD model including the SWIFT test article was developed. Minor simplifications were made to model, including removal of the starboard strut and the entire tail structure. Since these components would not have an effect on the flow-field around the SWIFT model, they could be safely removed, resulting in less computational requirements.

Using the CAD model of the O-2, a hybrid computational mesh was developed. Rhodes [19] provides an extensive explanation of the O-2 computational mesh development. Since an unstructured mesh is unable to resolve a three-dimensional boundary layer without demanding an enormous cell count, a structured mesh was needed for any boundary layer modeling. Therefore, a structured mesh was used for the region around the SWIFT model. However, such mesh fidelity was unneeded outside of this critical region; therefore, an unstructured mesh was used for the remaining portion of the O-2. The unstructured mesh was also able to better resolve the complex geometry of the airplane. For the outer free-stream region around the aircraft, another structured mesh was created. The O-2 mesh can be seen below in Fig. 11. This technique allowed the domain to extend well beyond the aircraft without incurring a large cell count. At the locations where a structured region met an unstructured region, a grid interface was defined. This allowed the CFD solver to pass information from one region to the other. This hybrid mesh technique proved to be extremely valuable in the CFD process, as it allowed accurate results to be obtained without demanding an unrealistic amount of mesh elements.

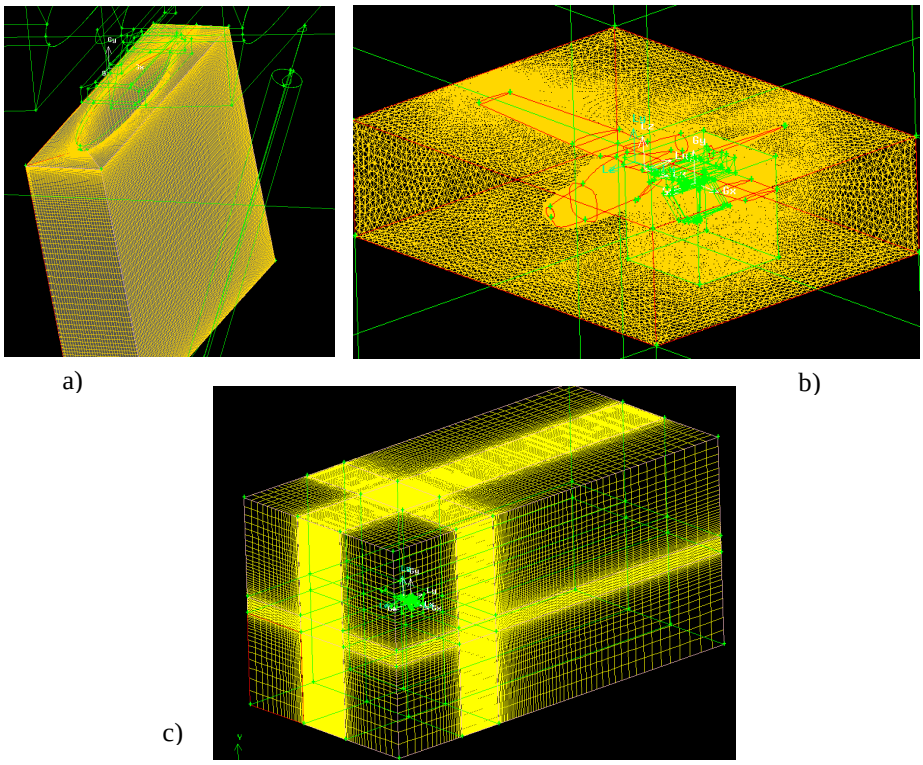

Fig. 11 Computational mesh for O-2 and SWIFT [19]. a) Structured region around SWIFT. b) Unstructured region around O-2. c) Structured free-stream region.

Other lessons were learned from the O-2 flight testing work as well. Flight data for the SWIFT model was taken from a five-hole probe mounted on the pressure side of the model. This probe was capable of measuring total pressure, static pressure, α, and β. The measurements from the five-hole probe were then used in the CFD cases in order to match the flight conditions. However, specifying the measured α and β as the boundary conditions for the computational model produced Cp data on the SWIFT that did not match the flight Cp. After an extensive CFD investigation, it was discovered that the flight conditions measured at the five-hole probe were not the same as the upstream conditions due to streamline deflection from the O-2 fuselage.

To remedy this issue, the free-stream velocity components at the boundaries for the CFD cases needed to be "backed-out" from flow-field data taken at the location of the probe tip. The upstream velocity components were adjusted until α and β at the location of the probe-tip matched the flight data. This

required multiple iterations for each set of flight conditions, as α and β were interdependent. However, once proper upstream conditions were determined, the excellent data agreement shown previously could be obtained.

4.2 Processing Platforms

The CFD studies were performed using the commercial FLUENT [20-21] CFD software package. Preliminary work was done with the FLUENT 6.3.26 version; however, FLUENT 12.0.16 was purchased in the fall of 2009 and subsequently used for all CFD work. The newer version had minimal differences compared to the older version, most of which were simply cosmetic. GAMBIT 2.3.16 [22] was used for creating the computational mesh for FLUENT.

All work performed to create the computational mesh was performed on an Apple Mac Pro personal workstation. The workstation used an open-source Linux operating system and had two Intel Xeon X5482 quad-core 3.2GHz processors and 32 GB of memory. The case setup within FLUENT was also performed on this machine. However, due to the complexity and high computational demand of the solution calculation in FLUENT, all cases involving the full aircraft model were run on the supercomputer Hydra at the Supercomputing Facility at Texas A&M. Hydra allowed parallel jobs utilizing up to 32 processors to be run with FLUENT. This significantly aided in obtaining solutions for several different cases in a timely manner. Technical specifications of the Hydra system are listed below in Table 3.

Table 3 Hydra system specifications.

Operating System	AIX 5.3
Processors	IBM Power5+ 64-bit
Total Number of Processors	832
Total Memory	1632 GB
Total Disk Size	20 TB

4.3 Meshing Techniques

4.3.1 General Process

The creation of a computational mesh for a CFD study involves many different elements. A balance must be struck between a highly refined and complex mesh and a coarse mesh requiring very little resources. Ultimately, a viable mesh must be able to capture all necessary physics while requiring the least amount of computational resources. However, the steps for achieving this goal are not always evident. Creating an efficient mesh can be considered an art; there are not always clear rules for the process. Often times, a mesh will go through several iterations before a satisfactory one is created. An overview of recent advances and different techniques for whole-body aircraft CFD grid generation and simulation is given by Agarwal [23].

To create a computational mesh in GAMBIT, several steps must be taken. First, edge meshes are created for the edges of the model. These represent the basis for the computational mesh. Many different options are available for creating edge meshes. Standard, constant-size edge meshes are the most common. These allow either a node-spacing specification or a node-count specification on the edge. However, other useful options also exist. An exponential distribution can be used, which clusters mesh nodes at one end of an edge and then increases the spacing exponentially towards the other end. A first-length option can be used that specifies the initial spacing of the nodes at one end, allowing the mesh to match neighboring meshes. Further along the mesh, the node spacing may increase. The exponential and first-length options are very useful for creating structured meshes around a wing. Fig. 12 shows an example of the first-length edge mesh for a wing surface. The elements along the surface and near the leading edge are the smallest, allowing small details of the flow to be captured. Further away from the surface and leading edge, the element sizes increase since less detail is required in this region.

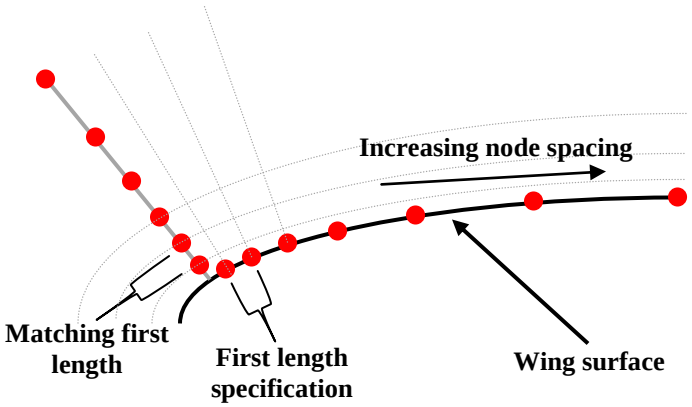

Fig. 12 Representation of edge mesh using first-length specification.

Using the edge meshes, two-dimensional face meshes can then be created. Growth rate functions can be specified for the face meshes, allowing the cell sizes to incrementally increase away from any edge meshes that are sourced in the function. This reduces not only the cell count for the face meshes but also the number of cells in the subsequent volume mesh. Attention must be paid during this stage, as poor face meshes will only be intensified in the volume meshes.

Growth rate functions can also be specified for the volume meshes. Using the faces as the sources, the cell sizes for the volume mesh can increase further away from the faces. The volume meshes represent the final step in the actual grid creation for the model. Following this, boundary types and continuum types must be defined.

4.3.2 Creating the G-II Mesh

Since only half of the G-II aircraft was used for the CFD study, a plane of symmetry was utilized. This method halved the computational requirements by assuming symmetric flow on the port and starboard sides of the aircraft. A vertical face cutting through the center of the fuselage was created to serve as this plane of symmetry. As anticipated, the meshing process for the G-II model required numerous iterations. Building upon the technique developed for the O-2 study, a hybrid mesh consisting of several different volume mesh zones was created for the G-II. The zones consisted of a free-stream volume, an aircraft volume, and a wing volume, shown in Fig. 13. Again, this setup permitted high-fidelity meshes in regions

of interest without having needless detail in less important regions. Each zone will be described, starting from the interior of the computational domain and working outward.

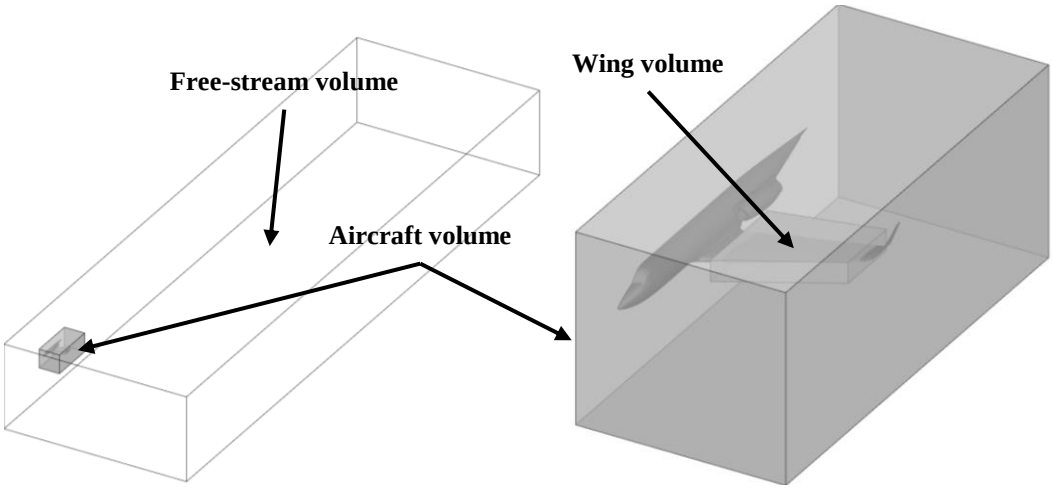

Fig. 13 Overview of G-II hybrid mesh setup.

The wing volume zone contained most of the aircraft wing. Since details of the pressure field on the wing were a key factor in this study, a high-fidelity mesh was preferred near the surface. A structured mesh around the wing would be able to achieve this required level of detail without incurring an unnecessarily high cell count. For the edges running along the leading edge of the wing, small node spacings were specified. The edges perpendicular to the leading edge running streamwise along the wing had edge meshes with a first-length spacing specification. The mesh spacing then slowly increased further aft of the leading edge. Normal to the wing surface, the mesh spacing was initially very small and slowly increased as the distance from the surface increased. The small element sizes near the surface allowed the flow to be adequately resolved. Fig. 14 shows the structured wing volume mesh created for the G-II.

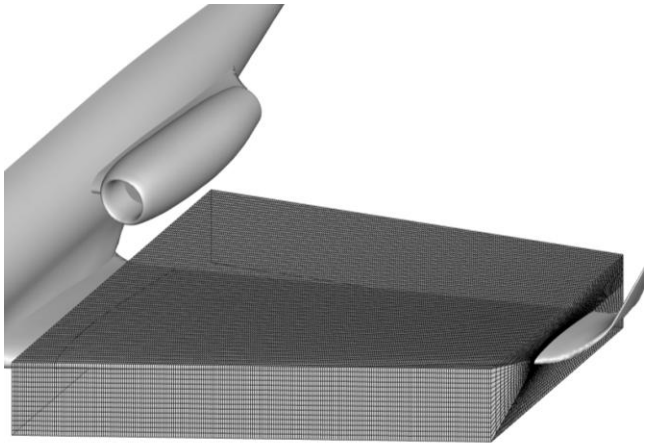

Fig. 14 View of the wing mesh zone.

The next zone was the aircraft volume, which actually contained the wing volume. The G-II model contained several complex geometrical features, necessitating an unstructured mesh since creating a structured mesh for such complicated geometry would be nearly impossible. All remaining parts of the aircraft not contained in the wing volume zone had a tetrahedral surface mesh. Since the aircraft surface was present in the structured wing zone and the unstructured aircraft zone, its surface mesh contained both types of elements, which is shown in Fig. 15. A growth rate of ten percent was specified for the aircraft volume mesh, allowing the cell sizes to increase as the distance from the aircraft surface increased. Much care needed to be taken during this meshing process, as the likelihood of highly skewed elements increased due to the complexity of a tetrahedral mesh. With several regions of the G-II model containing very small face and edge meshes, skewed elements could appear if neighboring regions had much larger face and edge meshes. Avoiding this required both user experience and multiple iterations of the meshing process starting with the edge meshes. The aircraft volume mesh can be seen in Fig. 16a.

Since minute details of the flow were not needed in regions far from the aircraft, a structured volume mesh was again used for the free-stream zone. Just as with the O-2 mesh, this allowed the far-field details of the flow to be modeled without causing a high cell count. This structured mesh was tailored so that as the distance from the unstructured volume mesh around the aircraft increased, the cell sizes increased as

well. The dimensions of the free-stream zone needed to such that any boundary effects would not affect the solution. Placing any boundary too close to the aircraft geometry could skew the flow-field results. The free-stream mesh can be seen in Fig. 16b.

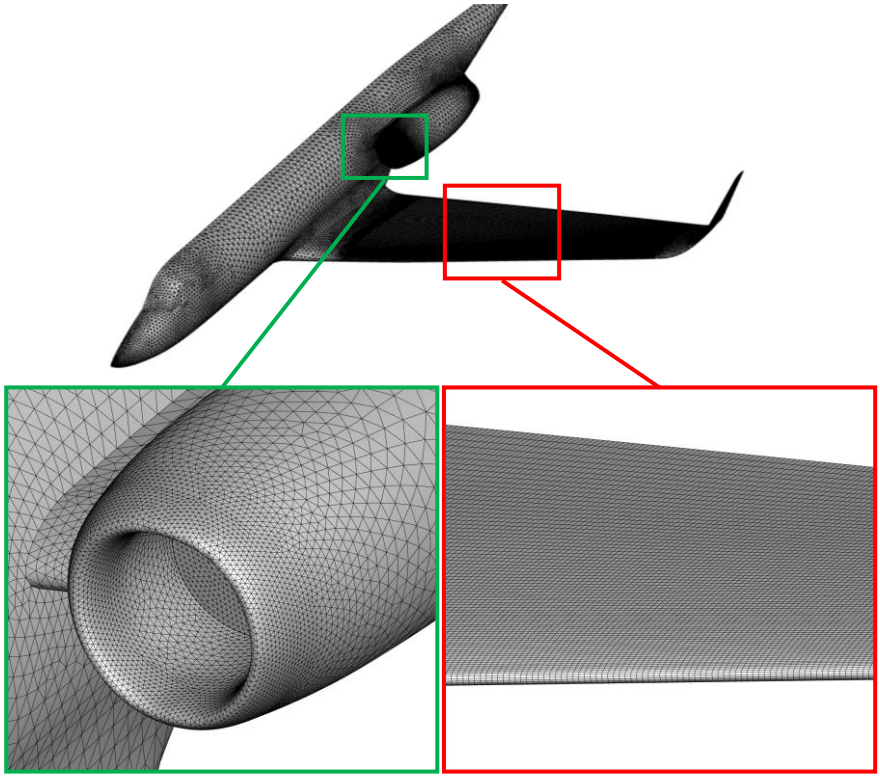

Fig. 15 Surface mesh of aircraft with unstructured and structured elements.

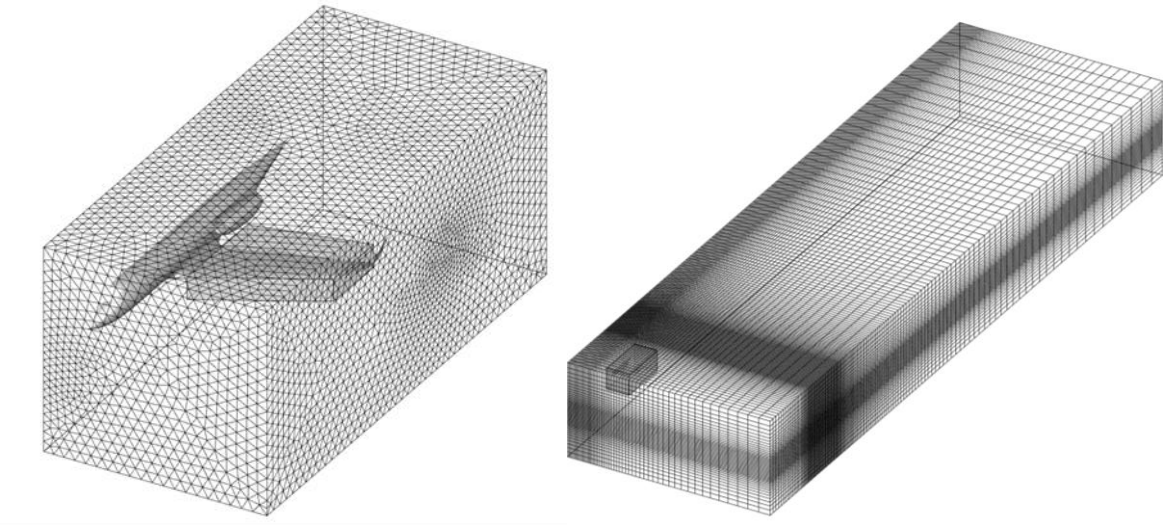

a) b)

Fig. 16 Views of the outer mesh zones. a) Aircraft mesh zone. b) Free-stream mesh zone.

At the locations where a structured zone and an unstructured zone interfaced, care was taken to match the cell sizes as closely as possible. This interface consisted of two different faces, one with a structured mesh and the other with an unstructured mesh, that existed in the exact same location of the computational domain. While the cell sizes do not need to match exactly between the two zones, more accurate flow-field results can be attained through this matching. These interfaces occurred in two locations. The first was the interface between the wing mesh zone and the aircraft zone, and the second was between the aircraft mesh zone and the free-stream mesh zone.

The final computational mesh consisted of over 4.2 million cells, with the majority coming from the unstructured aircraft mesh. While this was a significant amount of cells, it was still less than the number of cells in the O-2 mesh. The use of structured elements for the free-stream volume dramatically reduced the cell count in the mesh. Table 4 shows the different cell counts for each mesh zone. The entire domain extended 750 ft. in the streamwise direction, with the aircraft residing in roughly the front quarter of the span. The spanwise dimension of domain extended about 120 ft. from the centerline of the aircraft. The

domain extended about 100 ft. both below and above the aircraft. Grid convergence studies explained later indicated that these dimensions were sufficient for a solution.

Table 4 Cell counts for the different meshes.

Zone	Cell Count
Wing Mesh (Structured)	911,250
Aircraft Mesh (Unstructured)	3,176,254
Free-stream Mesh (Structured)	420,600
TOTAL	**4,508,104**

5. CFD CASE SETUP AND RESULTS

Performing a CFD study of an entire aircraft involves an enormous amount of processing power and time. The use of commercial codes such as FLUENT can often give the user a false sense of security. Improper solver settings and a lack of understanding of the problem can still produce results, but these would ultimately be useless. A strong knowledge of the basis behind the different solver settings in FLUENT is not only useful but necessary.

5.1 Boundary Conditions and Material Properties

Once the G-II computational mesh was imported into FLUENT, boundary conditions were specified. Initial targets for the flight test were a speed of Mach 0.75 at 40,000 ft.; therefore, these were the conditions specified for the CFD study. The five outer faces of the computational domain were defined as far-field pressure boundaries. The FLUENT User's Guide recommends this boundary condition for compressible, external flows. The boundary condition required a Mach number and direction vector specification, as well as an absolute static pressure and temperature. Using U.S. Standard Atmosphere 1976 values, the values used were a static pressure of 393.12 psfa and a static temperature of 390° R. The sixth face of the domain was simply defined as a symmetry plane. Table 5 lists the free-stream conditions that were specified in FLUENT for the CFD cases. A journal file can be created to specify parameter values at each boundary in the model, and this can then be read by FLUENT to quickly assign values for each boundary. This can save time during the setup stage and allows the user to rapidly update any values for the next CFD simulation. An example of this file is found in Appendix B.

Table 5 Free-stream conditions specified for CFD model.

Parameter	Value Specified
Mach No.	0.75
Static Pressure	393.12 psfa
Static Temperature	490 R
Air Density	Ideal Gas
AoA	0°

At the locations where unstructured mesh regions connected to structured mesh regions, grid interfaces were created. This feature allows FLUENT to pass flow information between two interface zones that do not have matching meshes. These grid interfaces were created for the interfaces between the wing mesh and airplane mesh and the airplane mesh and free-stream mesh.

FLUENT provides an option for specifying an operating pressure. This typically is set as the average absolute pressure of the flow regime and all pressures specified in FLUENT are in reference to this operating pressure (making them gauge pressures). By adding the operating pressure to the gauge pressures reported by FLUENT, the absolute pressure is determined, as seen in Equation 1. This is done to avoid numerical round-off errors in FLUENT. However, for higher-Mach number flows, it is recommended to set this operating pressure to zero, thus making all specified pressures absolute. Pressure changes in higher-speed flows are often large enough that round-off errors do not pose a problem. Therefore, for the G-II CFD study, the operating pressure was set to zero.

$$p_{abs} = p_{op} + p_{gauge} \tag{1}$$

Material properties for air also needed to be defined for the CFD study. Since the operating conditions were in the compressible regime, a constant density specification for air would not be possible. For compressible cases, FLUENT recommends the ideal-gas option for determining the air density. The ideal-gas law used is seen in Equation 2. Since the operating pressure was set to zero, the numerator simply becomes the absolute pressure calculated by FLUENT.

$$\rho = M_w \frac{p_{op} + p}{\bar{R}T} \tag{2}$$

5.2 Engine Modeling

Other important boundary conditions were the inlet and outlet of the engine nacelle. Boppe [24] explained the spillage and blockage associated with the engine's inlet can propagate on to an aircraft's

wing. These engine effects are particularly evident in business-jet type aircraft, since their nacelles are typically positioned near the root of the wing. Since flow-field disturbances on the wing caused by the engine could dramatically affect the wing glove placement, it was vital to the experiment to determine the extent of any engine effects. While a flow-through model did not require any boundary condition, as there were no faces at the inlet or outlet, the closed nacelle model needed a suitable condition specified at the fan face and the exhaust. In order to fully understand what needed to be modeled in the CFD study, some background research involving aircraft engine components was needed.

As explained in Flack [25], the first component of a turbofan engine is the diffuser, or inlet. The primary purposes of the diffuser are to deliver a smooth and uniform flow of air into the compressor and to decrease the air velocity to a speed suitable for the compressor. Mattingly [26] explains that an engine compressor typically operates best with a flow in the range of Mach 0.5. As a divergent channel, the diffuser uses its aerodynamic properties to accomplish the reduction in flow velocity to the on-design condition of about Mach 0.5, thus increasing the static pressure of the flow. This increase in static pressure caused by the diffuser represented a primary area of interest for the project, as this could affect the pressure distribution across the G-II wing. It was important to be able to model both the aerodynamic effects of the engine inlet as well as the fan face. By placing the boundary condition on a plane near the location of the engine's fan face, the flow would be able to naturally develop in the diffuser before reaching the boundary. With this in mind, an appropriate boundary condition at the fan face inside the engine was needed to model the effects of the engine.

The best option in FLUENT for modeling this pressure increase is the pressure outlet boundary condition. The FLUENT User's Guide recommends this boundary condition for flow exits in a compressible simulation. The pressure outlet boundary condition contains two different options that could be used to model the desired pressure increase. One method is to simply specify a static pressure at the boundary, which would represent the anticipated pressure increase within the engine that could potentially propagate upstream and on the wing. A rough correlation formula that uses the inlet pressure and Mach number to determine a typical fan face static pressure could be used to determine this pressure value.

However, this remained a rough estimation at best, and a more accurate condition for the fan face boundary was needed.

The second method, which was considered more appropriate for modeling the effects of the engine, involved using the pressure outlet boundary to specify a target mass flow rate at the fan face. Chen et al. [27] used this technique of specifying a mass flow rate at the engine's fan face for aircraft CFD simulations involving turbofans. With this boundary condition, FLUENT would adjust the static pressure value at the boundary for each iteration until it achieves the target mass flow rate. The change in pressure after each iteration was determined using Equation 3. This iterative technique for achieving a target mass flow rate at the fan face was also employed for turbofan CFD simulations done by Uenishi et al. [28]. Since this second method determines the pressure at the boundary using a target mass flow rate that would be appropriate for the G-II engine rather than requiring a set pressure value, it was considered more representative of the actual turbofan. Based on the explanation in Mattingly, the specified mass flow rate at the fan face should eventually bring the flow velocity to about Mach 0.5 under ideal, on-design conditions.

$$dP = 0.5\rho_{ave}\left(\dot{m}^2 - \dot{m}_{req}{}^2\right)/\left(\rho_{ave}A\right)^2 \tag{3}$$

To utilize this boundary condition, an appropriate mass flow rate was needed for the G-II engine. Seddon and Goldsmith [29] explain that during cruise conditions, aircraft engines typically operate in a "spillage" mode, which indicates the nacelle does not accept the entire flow at the inlet. This leads to a typical mass flow ratio (MFR) between 0.8 and 0.5 for the engine inlet [30]. The MFR is defined as simply the ratio between the mass flow actually accepted and the ideal mass flow based on engine inlet area and no flow blockage, shown in Equation 4. Thus, between 20 and 50 percent of the flow is typically blocked during ordinary cruise conditions. Boppe [31] reinforced this by specifying an MFR of 0.66 for CFD simulations investigating inlet flow rate effects of a G-III aircraft. Therefore, MFR values between 0.5 and 0.8 were considered appropriate for the G-II CFD cases.

$$MFR = \frac{\dot{m}_{actual}}{\dot{m}_{ideal}} \tag{4}$$

With these facts in mind, a strategy was developed for determining suitable mass flow rates for the engine. Using the inlet diameter of the engine shown in red in Fig. 17, the inlet's cross-sectional area was determined to be 4.79 ft^2. Based on this area, the ideal mass flow rate would be about 65.5 lbm/s for flight conditions of Mach 0.75 at 40,000 ft. However, as previously stated, the engines should not accept this entire flow during cruise conditions. This leads to an effective capture area of the engine that is less than the actual inlet area. By specifying different MFR values at the fan face boundary, the effects of the engine accepting less than the ideal flow rate could be modeled. It should be noted that this inlet area is not based on the slightly larger leading edge diameter of the inlet, also shown in Fig. 17. If the ideal mass flow rate was based on the leading edge diameter of the inlet, it would be about 80 lbm/s. However, by using the lower ideal mass flow rate of 65.5 lbm/s for the MFR values, a more conservative approach to the simulation of the engine could be used. Therefore, all subsequent references to MFR values are with respect to the mass flow rate of 65.5 lbm/s.

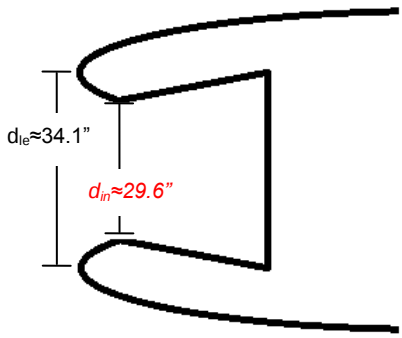

Fig. 17 Nacelle diameters. Red denotes diameter used for MFR values.

For initial calculations, simple CFD cases consisting of only the G-II engine were created. The flow-field domain for these cases was a simple rectangular domain with far-field pressure boundary conditions

on the sides. Operating conditions were again specified at Mach 0.75 at 40,000 ft. Multiple cases with different MFR values at the inlet , as well as a flow-through nacelle case, were created. The flow-through nacelle solution was used to examine the aerodynamic effect on the pressure field caused only by the engine's inlet. After obtaining a converged solution, the mass flow rate passing through the engine of the flow-through nacelle model was found to be roughly 52 lbm/s. This value was less than the unobstructed value due to the effects of the inlet. While the flow was still able to move through the entire engine nacelle and exit the back, the velocity was still reduced at the inlet. The reduced flow rate was thought to be partially due to the effects of the diffuser in the front of the nacelle. However, further within the nacelle, the geometry was not representative of the true engine, and the flow was not being properly modeled by the CFD results. Only the outermost part of the diffuser was actually scanned, so simplifications were made further inside the diffuser of the computational model. However, this model provided some guidance for the subsequent closed nacelle cases. Even without a boundary at the fan face, about 20 percent of the flow was still being blocked, indicating that the closed nacelle cases should have lower mass flow rates than the flow-through nacelle case since the effects of the fan face will also be included.

Next, mass flow rates were specified at the fan-face boundary of the closed nacelle model. MFR values of 0.8, 0.6, and 0.5 based on the unobstructed mass flow rate of 65.5 lbm/s were used for the simulations. This boundary was created by offsetting the inlet plane two ft. aft of the inlet, based on measurements taken on a Spey Mk 511-8. The same process was used to create this fan face boundary in the full-aircraft model. The MFR of 0.5, equating to only 32.8 lbm/s, represented the worst-case scenario, as it allowed the least amount of flow to enter the engine. Anything worse than this case should not be encountered during cruise conditions. However, having such an extreme condition can help bracket the effects of the engine on the wing. The results from the three closed nacelle cases and the flow-through nacelle case were then examined to determine the effects of different MFR values on the static pressure near the engine.

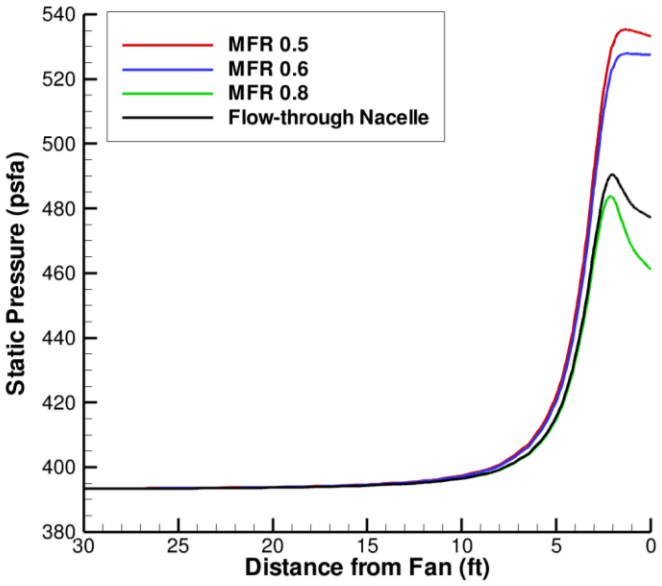

Fig. 18 Static pressure plots of the four engine models.

As seen above in Fig. 18, all four cases exhibited similar behavior near the fan face. The pressure values were taken along a line that passed through the center of the nacelle and travelled far upstream. The flow-through case and the 0.8 MFR case caused the lowest pressure increases since they accepted the highest mass flow rate. These two cases are very similar because both allow about the same amount of flow to enter. The other two MFR cases show much higher pressure increases due to their lower mass flow rates. The pressure increase can also be seen to propagate upstream, indicating that it could have an effect on the pressure distribution of the wing.

To confirm the validity of the different MFR values used, the Mach number of the flow at the fan face was also examined. As previously mentioned, compressors typically operate best with incoming flow at about Mach 0.5. Therefore, it was assumed that during standard cruise conditions, the flow should ideally enter the compressor of the G-II engine in this Mach range. The results of the CFD cases showing the fan face Mach numbers are shown in Fig. 19. The 0.8 MFR solution showed the flow velocity at the fan face to be about Mach 0.55, while the 0.6 MFR solution had a fan face Mach number of about 0.4. This

indicated that the on-design, cruise condition of the G-II turbofan should be an MFR between 0.8 and 0.6. From the plot, an MFR of about 0.73 should result in the ideal, on-design fan face velocity of Mach 0.5.

The fan face Mach numbers can also be extended to the higher ideal mass flow rate case based on the larger leading edge inlet diameter. Operating at Mach 0.75, the aircraft would be flying relatively near its maximum speed. Therefore, it would be expected that the engine would be operating at the lower end of the MFR range. If the higher ideal mass flow rate based on the leading edge diameter of the inlet were used for the MFR values, the 0.6 MFR would actually only equate to about 50 percent of the flow entering the inlet. With a fan face Mach number of 0.4 for this condition, the MFR would need to be slightly higher to achieve the Mach 0.5 condition. Therefore, the expected MFR should be in the lower range for the G-II during cruise at Mach 0.75, as originally deduced.

These results confirmed that the 0.5 MFR case could be treated as the worst-case scenario, as it had a velocity of only about Mach 0.3 at the fan face. It was not expected that the flow would reach a velocity this low during actual flight. The anticipated MFR for cruise at Mach 0.75 was found to be about 0.73 based on the fan face Mach number. Also, the range of MFR values used for this study was confirmed as representing a reasonable range for simulating the effects of the engine on the flow-field. The results also allowed a better understanding of how the different specifications at the fan face boundary affected the solution.

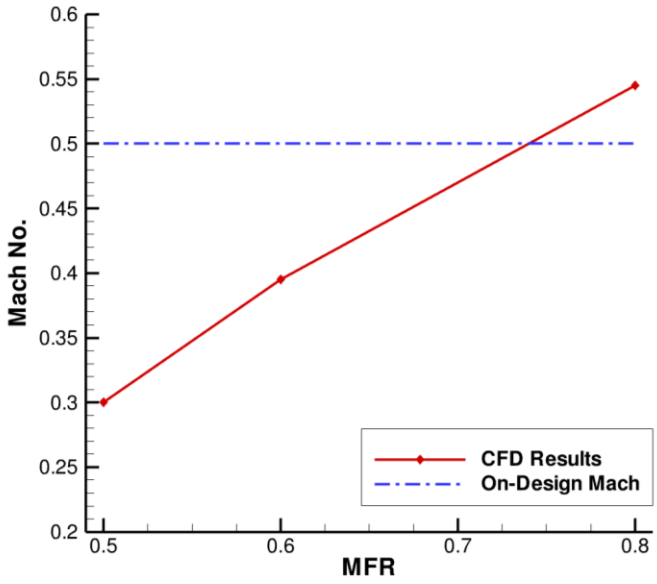

Fig. 19 Fan face Mach numbers at different MFR values.

With the inlet boundary condition determined, the engine exhaust was then examined for the closed nacelle model. The mass flow inlet boundary condition in FLUENT served as the most appropriate choice for this instance. The FLUENT User's Guide recommends this boundary condition as an inlet for compressible flows. Inputs for this boundary are a mass flow rate, a total temperature, and a static pressure. The static pressure specification is only used if the flow becomes supersonic; it is ignored if the flow remains subsonic.

The exhaust of the G-II engine is a convergent nozzle, and the flow exiting should be at a sonic condition. Therefore, ideally, the flow at the exhaust should be at Mach 1.0 in a converged CFD solution. Parameters that would primarily affect the Mach number of the flow at this boundary condition were the mass flow rate and the total temperature. This exhaust mass flow rate was specified for all closed nacelle cases, regardless of the mass flow rate specified at the inlet. While this did not technically obey mass conservation for the engine, it allowed the sonic condition at the exhaust to be maintained. Maintaining mass continuity through the engine would not affect the solution. Also, the cases with low mass flow rates

would not necessarily be realistic during flight, as they are simply worst-case scenarios used to determine the effects of a pressure rise at the inlet. Therefore, maintaining the sonic condition at the exhaust by keeping the mass flow rate fixed at 54 lbm/s was considered the most appropriate technique for the engine model. The assigned boundary conditions for the engine are detailed in Fig. 20.

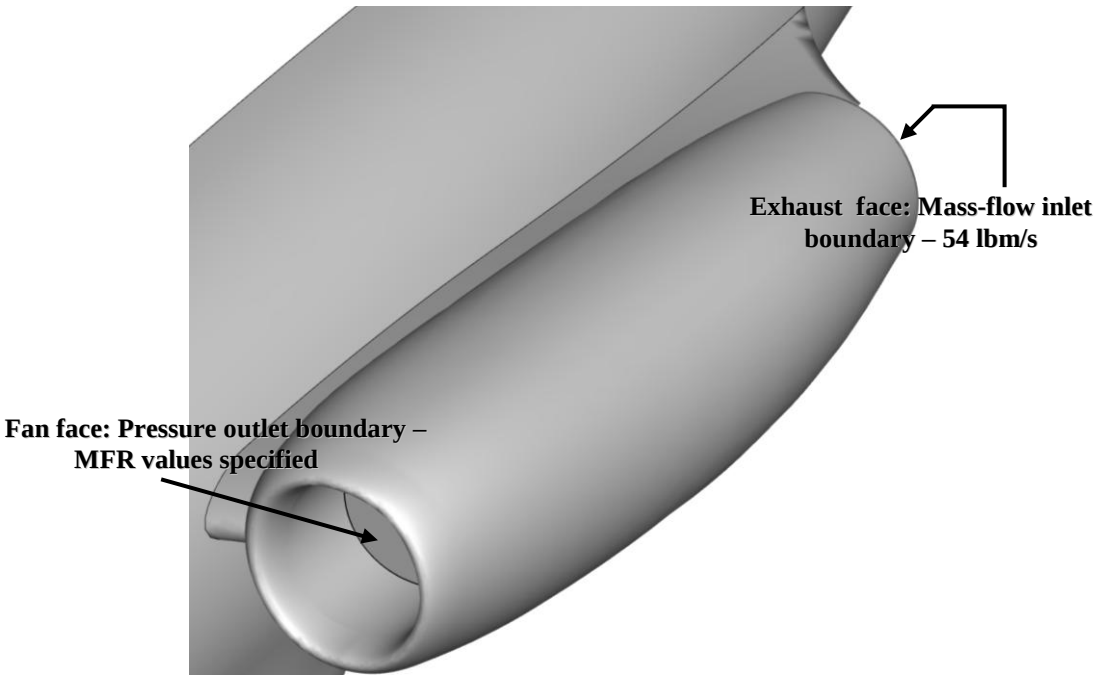

Fig. 20 Boundary conditions used for modeling the engine.

The simple engine models provided valuable information that was then applied to the full-aircraft models. A better understanding of the boundary conditions used and the aerodynamic effects of the engine was accomplished through these studies. Significant time was also saved by first modeling only the engine and then applying the lessons learned to the full-aircraft model.

5.3 Solver Options

Once the boundary and operating conditions were set, the solver options within FLUENT were examined. According the FLUENT User's Guide, the pressure based solver was initially developed for incompressible and mildly compressible flows. A density based solver is also included in FLUENT, and

this was originally used for high-speed compressible flows. While both solvers have been modified and extended for use in much wider-ranging flow conditions, the pressure based solver was used for this project since its original design was for flow conditions similar to the current test.

For the evaluation of gradients and derivatives, the FLUENT User's Guide states that a Green-Gauss Node-Based gradient evaluation method is the most appropriate for unstructured meshes. Since the computational mesh contains a considerable amount of tetrahedral cells, this method was used for all simulations. The SIMPLE algorithm was used for the pressure-velocity coupling method. While this algorithm often leads to slower convergence when compared to SIMPLEC, it is preferable for complicated problems with complex meshes. The other pressure-velocity schemes, the PISO method and Fractional Step method, were not appropriate for the problem, as they are recommended for transient problems.

Turbulence models were not used for the simulations. Rather, the laminar option under the viscosity selection was chosen. For discretization, first-order schemes were used for all convective terms of each governing equation. For the viscous terms, FLUENT automatically uses second-order discretization. While second-order discretization was recommended by FLUENT for the pressure interpolation for compressible flow, this option would further add to the computational requirements. Verification of using the first-order schemes is addressed later.

FLUENT uses under-relaxation factors in the pressure-based solver to help control updated variables for each iteration. This is done in effort to prevent any rapid divergence of variables. The FLUENT User's Guide states that the default values of the under-relaxation factors should suffice for most simulations. Once a suitable computational mesh was developed, the need for modifying any of these were eliminated, as convergence was reached with the default settings. A few tests were done with different under-relaxation factors, but these did not provide any advantage or affect the solution. Therefore, all results presented used the default settings.

To judge convergence, the scaled residuals were used. After each iteration, FLUENT calculates and stores the residual sum of the conserved variables in the solver. The FLUENT User's Guide explains the residual sum is then scaled by a representative factor of the flow rate through the domain. The default

convergence criterion requires the scaled residuals to decrease to 10^{-3}. This default value was used for nearly all of the CFD cases. Table 6 below details the final solution setup used in FLUENT.

Table 6 Solver settings.

Option	Value
Solver	Pressure-based
P-V Coupling Method	SIMPLE
Gradient Evaluation	Green-Gauss Node-Based
Viscosity	Laminar
Discretization	1^{st} Order
Residual Convergence	10^{-3}

5.4 Solution Strategies

Obtaining a converged solution for the previous work done on the O-2 was relatively easy once a computational mesh of satisfactory quality was created. However, a compressible simulation involving such complex geometry as the G-II proved to be much more difficult for obtaining a converged solution. With variable density and the inclusion of the energy equation in the simulation, much care needed to be taken in order to reach convergence. As expected, a high quality mesh was extremely important. Any highly skewed elements within the volume mesh could prove detrimental to the solution. Again, avoiding this required a thorough and patient mesh creation process within GAMBIT.

Despite such immense care taken during the mesh creation stage, other strategies were also needed in order to reach convergence. Initializing a simulation at a higher Mach number such as 0.8 typically caused rapid divergence within the solution calculation. With such complicated physics occurring, the solver was often unable to remain stable with such high-speed initial values. This prompted a technique of stepping up the flow velocity incrementally. First, a solution for the model would be obtained at a speed of Mach 0.3. Once convergence was reached, this velocity was increased to Mach 0.5. With a solution already obtained at the lower Mach number, the solver would remain stable during the velocity increase. Finally, after convergence at Mach 0.5, the final required Mach number, typically Mach 0.75, was used in the

simulation. This multi-step process, though slower, proved to be extremely successful in obtaining stable and converged solutions within the needed velocity range.

5.5 Results

Once the proper solver settings and boundary conditions were determined, solutions were obtained for the different full-aircraft CFD cases. Table 7 details the mass flow rates used for these cases based on the results from the nacelle-only CFD cases. The primary focus for the results was the pressure distribution on the wing. Disturbances from the engine could affect where the wing glove could be placed. By comparing solutions of the no-nacelle model to different cases of the closed nacelle model, the effect of the engine could be determined. Of importance is a relatively spanwise-constant pressure distribution. Such a distribution would provide a suitable location for the wing glove, as the flow would be mostly consistent. Interference from the engine could introduce atypical flow patterns on the wing, thus adversely affecting the wing glove flow-field.

Table 7 Mass flow rates specified for each model.

Model	Inlet Mass Flow (lbm/s)	Exhaust Mass Flow (lbm/s)
0.8 MFR	52.5	54
0.6 MFR	39.4	54
0.5 MFR	32.8	54
No-Nacelle	N/A	N/A

To view the effects of the engine on the wing pressure field, Fig. 21 and Fig. 22 show Cp plots at 25 percent and 45 percent span, respectively. The span percentage is taken with respect to usable wing span, i.e. the winglet was not included in the total span since the wing glove could not be mounted in this location. The 25 percent span plot is almost directly below the engine, thus causing the dramatic difference between the three MFR cases and the no-nacelle model. A much more adverse pressure gradient is present on the MFR cases, progressively worsening as the mass flow decreases. However, at 45 percent span the effects are much less noticeable. While the pressure gradient is still shallower, it closely resembles that of

the no-nacelle. These results indicate that further outboard, the pressure field may be suitable for the wing glove. While these plots show a local view of the engine effects, a more global view of the pressure distribution on the wing is necessary to draw more concrete conclusions.

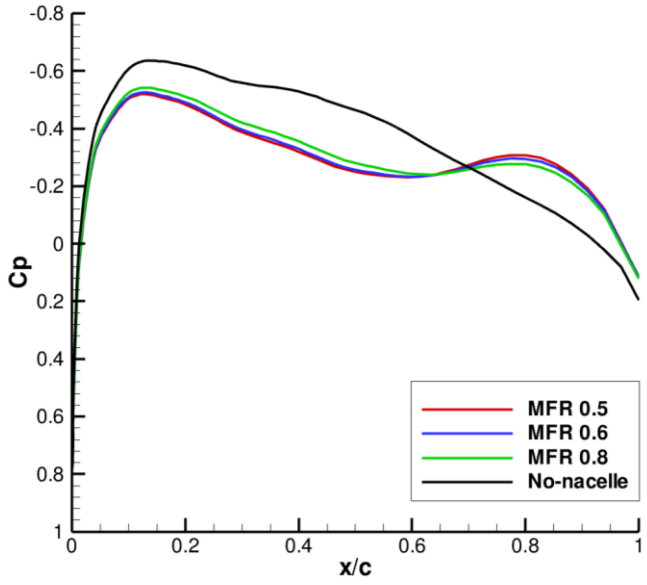

Fig. 21 Cp data at 25% span.

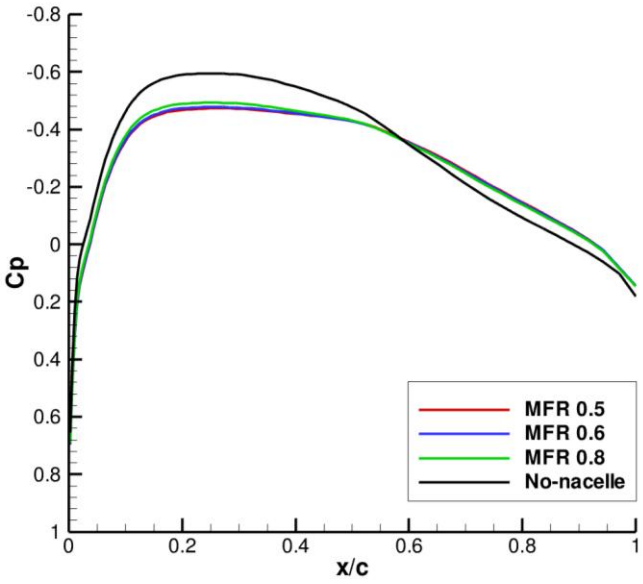

Fig. 22 Cp data at 45% span.

Presented first in Fig. 23 are the pressure contours for the no-nacelle model. The wing is delineated by in increments of 10 percent span. The pressure distribution is relatively spanwise constant, which is expected for a wing without any disturbances. Next, the results from the 0.8 MFR case are presented in Fig. 24. Notice the pressure changes on the wing near the engine inlet. As anticipated, the static pressure increase at the engine inlet propagated upstream and onto the wing. However, the effects are seen to dissipate further outboard on the wing.

Fig. 25 and Fig. 26 show the more severe closed nacelle cases. Again, an adverse pressure gradient is present in the immediate region by the engine inlet for these two cases, with the effects dissipating further outboard. Since the 0.6 and 0.5 MFR cases have a lower mass flow rate and, thus, a higher pressure increase than the 0.8 MFR case, the effects by the engine are more severe. Of note is the increase of the high-pressure region directly below the nacelle as the MFR is decreased. However, the high-pressure region mostly vanishes near the 40 percent span mark for all MFR cases.

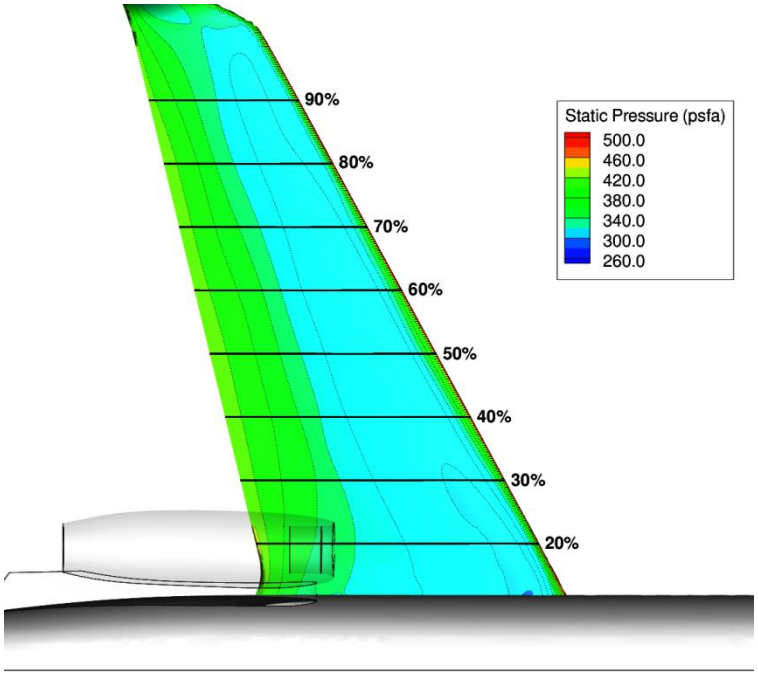

Fig. 23 Pressure contours for no-nacelle model.

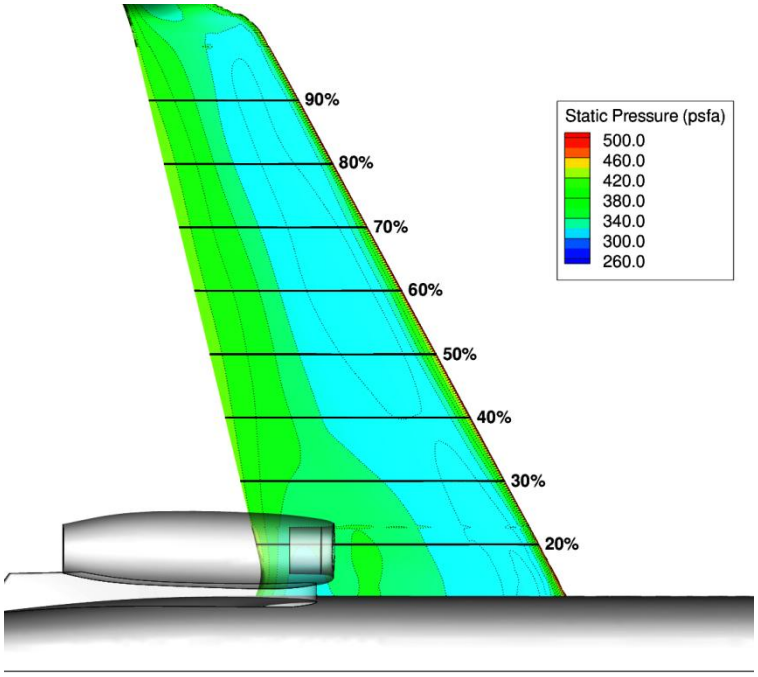

Fig. 24 Pressure contours for 0.8 MFR closed nacelle model.

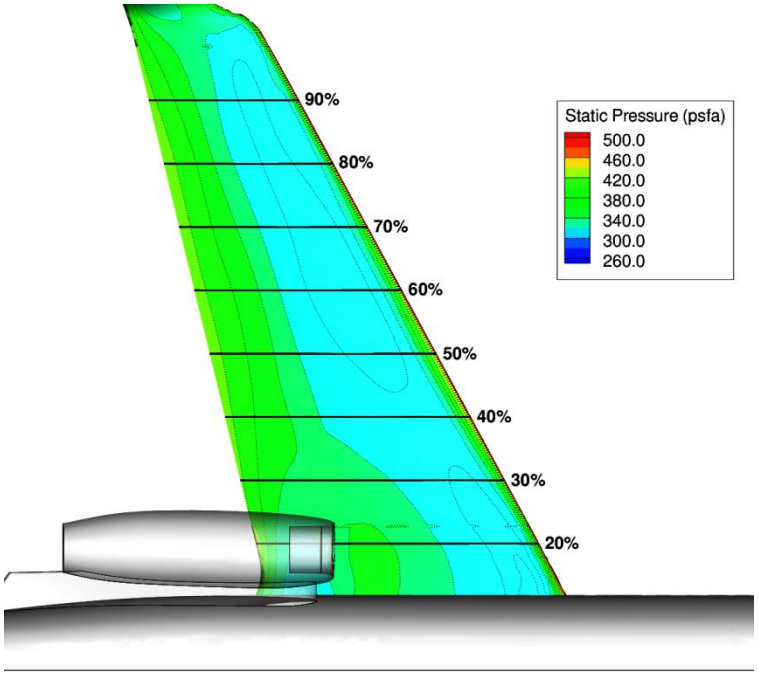

Fig. 25 Pressure contours for 0.6 MFR closed nacelle model.

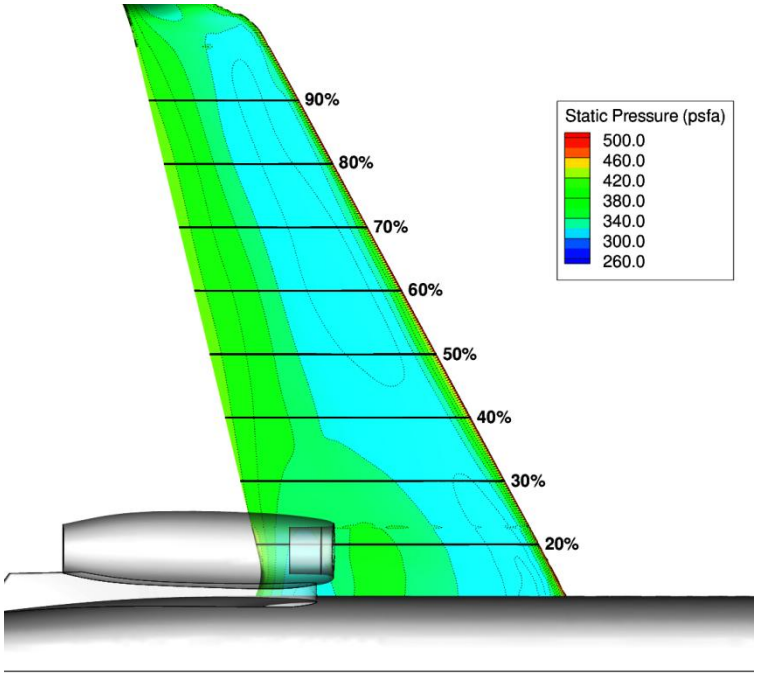

Fig. 26 Pressure contours for 0.5 MFR closed nacelle model.

Despite the marked influence of the engine on the inboard section of the wing, the pressure effects dissipate at about the same rate for all three closed nacelle cases. In fact, all three cases show a relatively spanwise-constant pressure distribution after about 45 percent span. These results indicate that after about 45 percent span, the pressure distribution on the wing can be expected to be relatively spanwise-constant, regardless of the mass flow rate of the engine. A close-up view of the pressure contours of the 0.5 MFR case showing the nearly spanwise-constant distribution is shown in Fig. 27. The red region represents the suitable mounting area for the glove, while the dotted blue lines show the spanwise-constant pressure contours. Since this is the worst-case model, any location outboard of 45 percent span should be suitable for the wing glove LFC experiment.

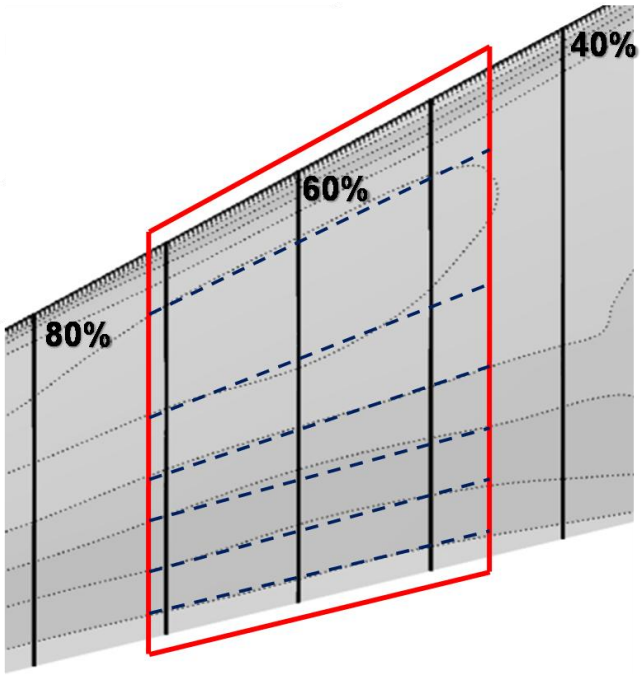

Fig. 27 View of spanwise-constant pressure lines on MFR 0.5 case.

To gain further insight into the flow-field around the engine and wing, the streamlines entering the nacelle were also examined. Shown in Fig. 28, the streamline cluster for the 0.5 MFR case expands as it approaches in the inlet, indicating the nacelle is blocking a percentage of the flow. Again, this helped

confirm the boundary condition used for the fan face, as the low mass flow rate specified was blocking a certain amount of the flow. Also of note is the change in static pressure as the streamlines approach the inlet.

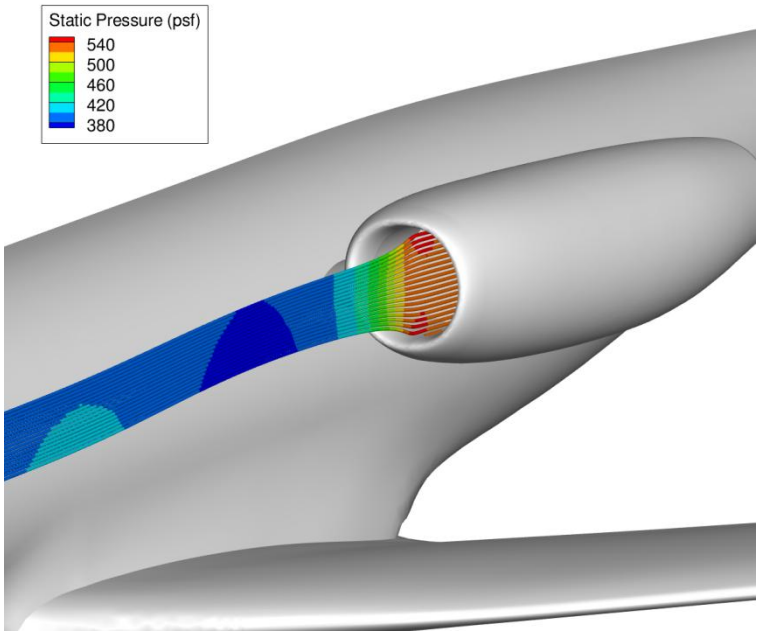

Fig. 28 Streamlines entering nacelle (colored by static pressure).

Next, the streamline deflection due to the fuselage was examined. As discovered in the O-2 work, the fuselage tends to alter the free-stream streamlines. Care must be taken when taking measurements of the flow-field so that they match what the wing glove is experiencing. To ensure this on the SWIFT model, the five-hole probe was mounted on the pressure side of the model so that it would experience as closely as possible the same flow-field qualities as the test side of the model. Due to the vertical orientation of the SWIFT, the aircraft β correlates to the SWIFT α. Correct α measurements were essential, as this parameter plays a large role in the receptivity and transition process. While the wing glove in this experiment will be mounted horizontally over the aircraft wing, which eliminates any angle conversion, the α and β the glove

experiences could still be slightly different from the actual aircraft α and β due to the presence of the fuselage.

For determining the streamline deflection, a setup similar to the SWIFT model was assumed. On the SWIFT, the five-hole probe used for measuring air data was positioned about six inches off the pressure side of the model, and its tip extended about two ft. upstream of the SWIFT leading edge. Therefore, the tip of the air data probe for the wing glove on the G-II was assumed to be six inches below the glove's pressure side and two ft. upstream of the leading edge. With a six foot wing glove mounted on the aircraft at about 45 percent span, the probe was assumed to be positioned at about 53 percent span. Velocity component measurements were taken along a horizontal straight line spanning the entire domain and passing through the estimated probe tip location. The probe tip was assumed to be about two ft. upstream of the wing leading edge.

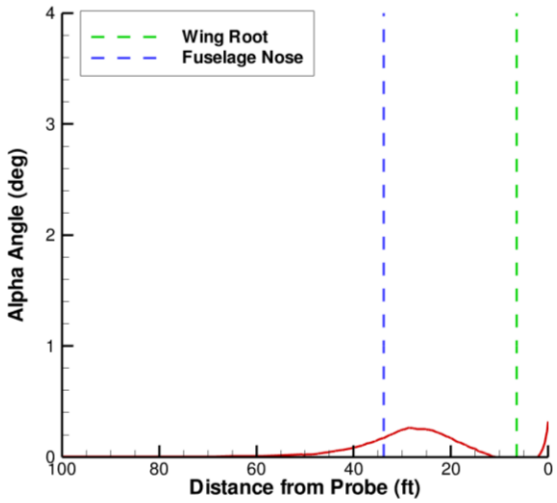

Fig. 29 Changes in wing glove α due to streamline deflection.

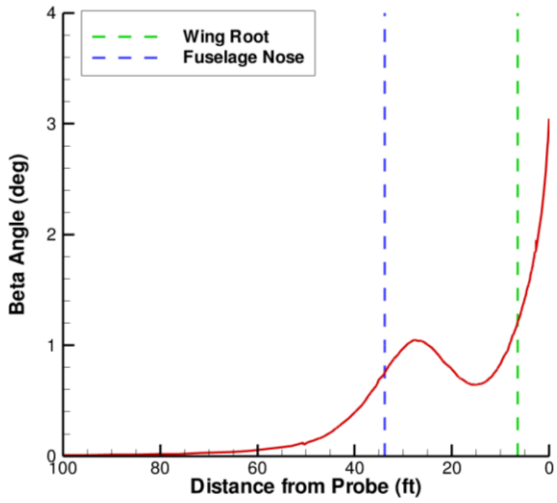

Fig. 30 Changes in wing glove β due to streamline deflection.

Fig. 29 shows the evolution of α as the flow approaches the probe tip. The location of the aircraft nose is represented by the dashed blue line, and the wing root location is shown by the green dashed line. Minimal deflection in α is experienced, which is expected. The fuselage should not have a significant effect on α, which is confirmed in the above figure. However, a greater deflection is experienced in β, as seen in Fig. 30. Again, this is expected, as the fuselage will cause the streamlines to bend away from the body, thus changing the β the wing glove will experience. This can be seen in the above figure, as β begins to increase as the flow approaches the aircraft nose. Roughly speaking, the wing glove should experience about a 3 degree increase in β due to the deflection. However, changes in β should have very little effect on the LFC experiments. Appendix C provides additional figures showing the streamlines over the wing.

5.5.1 Verification

A necessary step in a CFD study is the verification of the results. As explained in the AIAA Guide [32], verification involves determining if the computational model and its case setup accurately represent the user's conceptual model and its solution. FLUENT represents a widely-used commercial code that has been verified on numerous levels, and no issue was taken to the accuracy of the code itself. Therefore,

only the computational model created for the G-II needed to be verified. The following tests were performed to demonstrate that the options used in FLUENT for the final results presented were sufficient for obtaining accurate results.

One test for verification of the results involved determining if the boundaries of the computational domain affect the flow-field solution. If the boundaries are constructed too close to the aircraft, they can often influence the solution, skewing the results. To check this, another computational mesh was created for the closed nacelle model with boundaries extended in all five directions (no extension was needed nor necessary on the symmetry face). This was called the "Extended Grid." The interior meshes around the aircraft and wing remained the same as the ones used in the normal mesh version of the closed nacelle model. A solution was obtained at the same operating conditions as the original model, and Cp values along the wing were compared. Fig. 31 shows a comparison of Cp plots at 25 percent span, with at 45 percent span. As seen, the results are nearly identical, indicating the normal grid sufficiently models the flow without any effects from the boundaries.

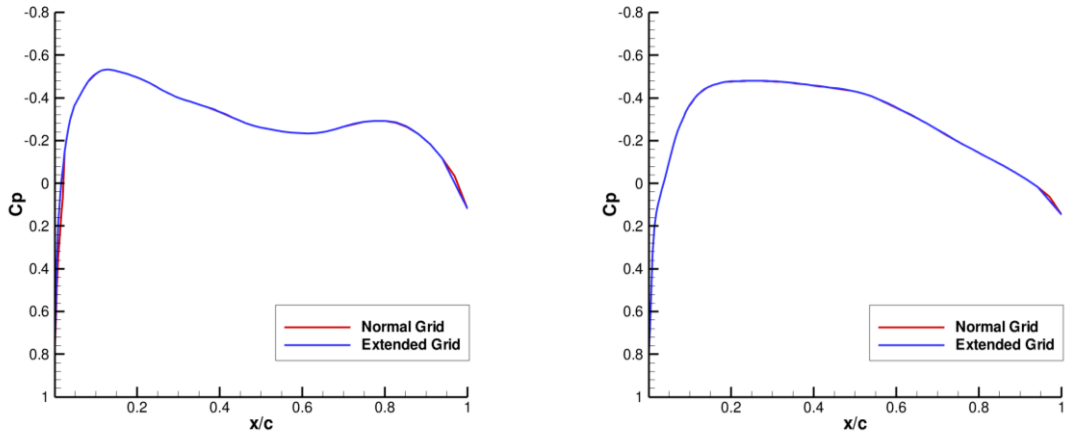

Fig. 31 Cp comparisons between the normal and extended grids. a) 25% span. b) 45% span.

Further verification was accomplished through comparing results of varying fidelity meshes. A grid refinement process can allow the solution to be considered grid independent if the results remain relatively

unchanged through different meshes. To check for grid independence, three different meshes were created for the closed nacelle model. The "Normal Grid" was the grid used for the results previously presented. A second one, called the "Fine Grid," had higher cell count around the wing and aircraft. A third mesh, called the "Coarse Grid," was the least refined of the three, having a much lower cell count. All three cases were run at the same conditions and the Cp values at different wing stations were compared. Figure shows the comparison of the three grids at two different wing stations. As seen in Fig. 32, the Normal Grid and Fine Grid yield nearly identical results. The Coarse Grid does not appear to resolve the pressure distribution as well as the other two, though the overall behavior is the same. This was expected, as the low cell count prevented the grid from fully capturing the physics. These results indicate that the Normal Grid was appropriately refined to capture the important physics of the flow-field. This enable computational time to be saved by not needed a higher-refined grid. This process was also repeated for the NEM, and similar conclusions were reached.

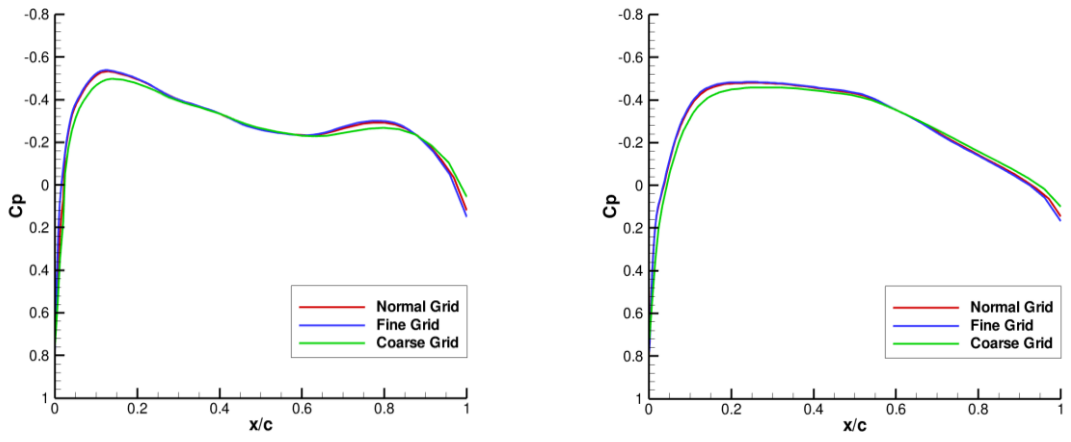

Fig. 32 Cp comparison between three different fidelity grids. a) 25% span. b) 45% span.

Another study was performed that examining different discretization schemes. First-order discretization was used for the results previously presented. To determine if a higher-order scheme would provide different results, a solution was obtained using second-order discretization for the pressure and

density interpolation schemes. Comparing the results from this higher-order solution to the base solution with first-order schemes would reveal any differences originating from different discretization. The Cp plots shown in Fig. 33 show that the first-order and second-order solutions are in excellent agreement. This indicates that the first-order scheme is sufficient for obtaining results, and the costlier use of higher-order discretization is unnecessary for this study.

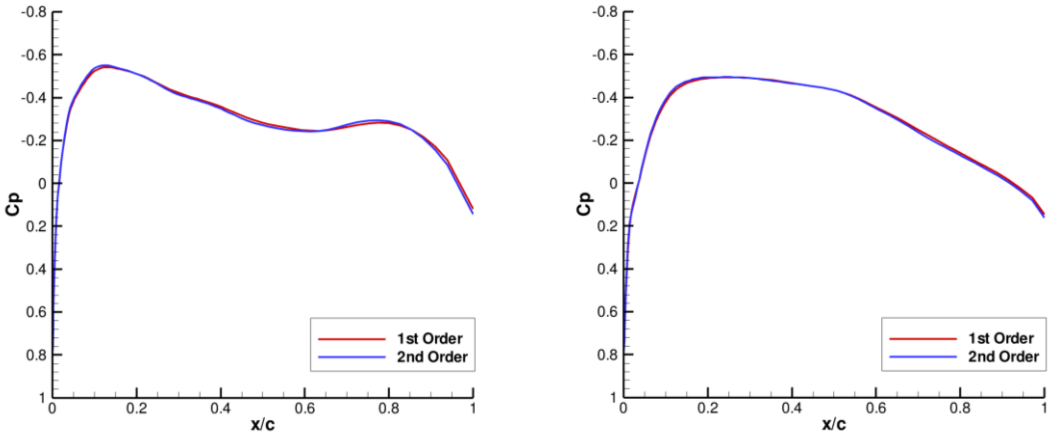

a) b)

Fig. 33 Cp comparison between 1st and 2nd order discretization. a) 25% span. b) 45% span

Finally, to determine if sufficient convergence had been reached for the results presented, another verification study was performed by obtaining a solution of closed nacelle model with convergence criteria increased to $1.0e^{-4}$ and $3.0e^{-5}$. By comparing the results of this higher converged model to the original closed nacelle model results using the default convergence criteria, any changes due to the modified criteria could be determined. As seen in Fig. 34, all three residual convergence criteria yield the same Cp plot at 25 percent span, indicating that the default criteria of $1.0e^{-3}$ is sufficient.

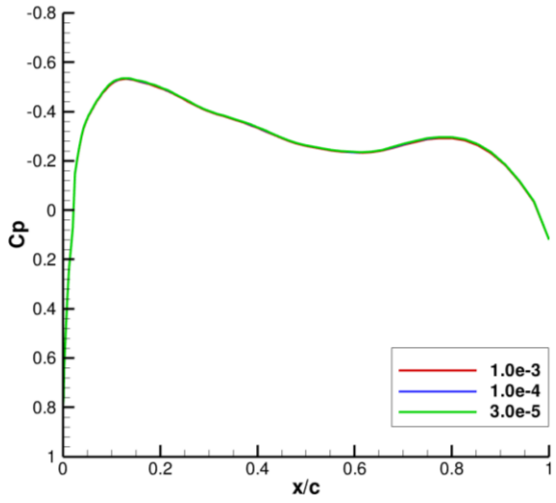

Fig. 34 Cp comparison between different residual convergence criteria.

5.5.2 Validation

Due to the lack of accessible experimental data for the G-II aircraft, validation of the CFD results was difficult. The previous success of computational data agreeing with flight data from the SWIFT experiments provides an extended validation of the process and techniques used for the aircraft CFD studies. It also provides validation to the FLUENT code. Nonetheless, this extension can only be taken so far, as the G-II CFD model was much more complex than that of the O-2A. Compressibility, a turbofan engine, and a higher velocity all added to the complications of the G-II computational model.

However, the exact details of the flow-field were not absolutely necessary for this study; rather, the general behavior of the flow near the wing was only needed. Therefore, if the modeling techniques used were able to capture the basic effects of the engine, then useful conclusions could be drawn from the solution. Qualitative comparison with the G-III wing pressure field results done by Boppe[26] shows relative agreement. In regions near the nacelle, the flow is decelerated in front of the inlet and slightly accelerated aft of the inlet. This same behavior was seen in the G-II results, with a “valley” in the Cp plot located mostly in the immediate region in front of the inlet. However, further outboard, the decelerated dip in the

Cp disappears, again agreeing with the G-II results. While actual numerical data was not used in this comparison, the overall behavior of the flow-fields for both studies was in relative agreement.

6. DISCUSSION AND CONCLUSION

6.1 Recommendations and Extension to the G-III

After analyzing the flow-field results from the CFD study, the selected G-II/SP is capable of performing the required flight tests. While the engine does appear to interfere with the pressure distribution on the wing, its adverse effects dissipate further outboard. The pressure distribution was seen to be relatively spanwise-constant after about 45 percent span. Therefore, mounting a wing glove outboard of 45 percent span would be recommended, as shown in Fig. 35. At this location, the streamline deflection should not be an issue. Angle of attack remains relatively unchanged, while the slight increase in β should not have any adverse affects on the wing glove.

The chord length of the G-II at 45 percent span is about 12.1 ft. Assuming a glove span of six ft., starting the wing glove at 45 percent span would cover the G-II wing up to about 60 percent span. The chord at this location reduces to about 10.7 ft. Therefore, using the average chord length of roughly 11.4 ft., the wing glove should be able to achieve a chord Reynolds number of about 16.4 million at Mach 0.75 and 40,000ft. Table 8 shows the changes in chord Reynolds number as the flight conditions are varied using the 11.4 ft. chord length. As seen, this location for the wing glove would be able to achieve the desired chord Reynolds number at numerous flight conditions.

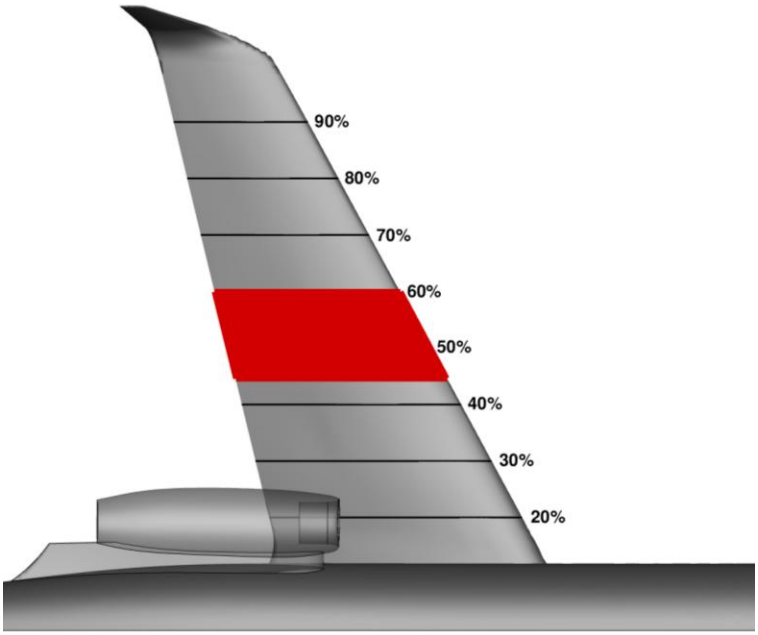

Fig. 35 Recommended location for wing glove (red).

Table 8 Chord Reynolds numbers at various conditions.

Mach No.	Altitude (ft.)	Chord Reynolds No. ($x10^6$)
0.75	40,000	16.4
0.75	30,000	24.4
0.70	40,000	15.3
0.70	35,000	19.1
0.70	30,000	22.8

As this project matured, the G-III aircraft emerged as the primary candidate for the flight tests. While it was unfortunate that this was not the selected aircraft initially, it in fact should serve as a better test bed. As mentioned in the Section 2, since the G-III has a larger wing, it is better equipped to attain the desired chord Reynolds number. Furthermore, since the G-III uses the same Spey Mk 511-8 engine, the results from the G-II study could be easily correlated to the G-III.

Rough measurements from three-view drawings indicate the G-III has a chord of about 13.2 ft. at 45 percent span. Assuming the same wing glove mounting location starting at 45 percent span and extending six ft. outboard, the G-III wing glove could theoretically achieve a chord Reynolds number of 17.4 million at Mach 0.75 and 40,000 ft. However, this is probably a conservative estimate. While the G-III wing is on a larger scale than the G-II wing, both aircraft have the same size engine. Therefore, it would be expected that the engine's adverse effects would only extend same distance but not necessarily the same spanwise percentage. The G-II model regained spanwise-constant pressure distribution just under 15 ft. from the centerline. This distance would only be at about 40 percent span on the G-III, thus providing a longer chord for the wing glove.

6.2 Future Work

Much work still needs to be performed for this LFC flight experiment. A new CFD study will need to be performed on a G-III model in order to obtain accurate flow-field details of this aircraft. The entire process discussed previously is expected to be repeated. An accurate laser scan of a G-III aircraft will be performed, allowing a CAD model to be created. This model will then be used to develop a computational grid for CFD studies.

Following the updated flow-field results of the G-III, a wing glove model will be added to the aircraft geometry. Similar to the work done on the SWIFT model, a boundary layer mesh will be created for the wing glove in order to obtain mean-flow results for stability analysis. This will result in a much more complicated mesh that will require plenty of patience and iteration. Once a solution is obtained and validated with flight data, the boundary layer mean-flow can be extracted from FLUENT. This will require the use of a UDF, as described in the O-2 CFD work. The mean-flow results will then be used for guidance in altering the glove design to attain the desired Cp, as well as information regarding DRE application on the wing glove. The most unstable wave-numbers and their neutral points will be calculated, thus determining the proper placement of the DREs.

However, the work done on the G-II provided a valuable reference and background for the project. Proper techniques for creating a CAD model from scanned data points were developed, and efficient

methods for creating a robust computational mesh were discovered through working with the G-II. An equally important aspect of the G-II work is the modeling of the aircraft engine. This served as one of the main reasons for conducting a CFD study, and the modeling of the engine's effects proved to be very successful. Based on the G-II CFD work, the following brief recommendations are made for future full aircraft CFD at transonic speeds:

1) Due to the compressibility effects associated with higher Mach numbers, the computational mesh must be created so that it can accurately capture the complex physics of the flow-field. The far-field boundaries must be placed far enough away from the aircraft so that they will not influence the solution. Highly skewed elements need to be avoided as much as possible to ensure convergence.

2) A simple technique for reducing the computational requirements for the problem is to create a plane of symmetry for the model, which cuts the aircraft in half at the centerline of the fuselage.

3) While verification efforts demonstrated that the computational domain boundaries were not significantly affecting the flow-field results around the aircraft wing, an even larger computational domain may need to be considered for future CFD work. This need can ultimately be attributed to the large effects on the flow-field produced by the mass flow inlet at the engine exhaust. The effects from this boundary condition extend far downstream and may not fully dissipate before reaching the back boundary. Precise flow-field details were not critical for the current work; therefore, it was not considered essential to create a large enough domain to allow the exhaust effects to complete dissipate before reaching the back boundary. Rather, the general flow-field results around the wing could still be determined with a smaller, more efficient domain. However, once the CFD results are needed for boundary layer data, a larger domain may be necessary.

4) An effective way to model the effects an aircraft turbofan engine has on the surrounding flow-field is using mass flow boundaries at the engine fan face and exhaust. On the inlet side of the engine, both the aerodynamic effects of the inlet lip and diffuser and the effects of the fan face inside the engine are important when modeling the nacelle since an increase in static pressure from the inlet can propagate upstream and onto the aircraft's wing. To represent the flow into the engine, a mass flow rate can be specified at the fan face boundary. Since aircraft engines typically do not accept the full flow rate during cruise conditions, the specified mass flow rate should be less than the ideal flow rate for the engine. For the exhaust boundary condition, the flow should be sonic. A proper mass flow rate and temperature specification are necessary for achieving this condition.

5) Convergence can be a difficult when initializing the CFD case at higher Mach numbers. An effective way to avoid this difficulty is to initialize the solution at a lower Mach number, such as 0.3. After obtaining a converged solution, the Mach number can be incrementally increased, using the previous solution for initialization. While this takes longer to a final solution, it is highly effective.

6.3 Concluding Remarks

Several lessons were learned throughout this feasibility study. What started as a simple extension of the CFD work done on the O-2A and SWIFT model turned into a completely different project with its own particular problems. The work performed answered the first two questions regarding the feasibility of using a transonic transport aircraft for an LFC flight experiment. Some of the lessons learned throughout the study are discussed briefly below.

The sensitivity of a wing's pressure field to surface geometry in aircraft CFD work was discovered. Simple aspects such as discontinuities between surfaces in a geometric model can have dramatic effects on the flow-field solution. Special care needed to be taken when creating the G-II CAD model so that geometry represented the actual aircraft as closely as possible. Access to actual flight data would assist in creating an accurate geometrical model, since surface discontinuities that are not present on the as-

designed model could exist on the actual aircraft. However, without sufficient access to flight data, it was difficult to verify whether the problems noticed on the Cp plot of the initial model of the G-II are artifacts of the CAD model or actual discontinuities on the physical aircraft. However, for the purposes required by this study, an ideal representation of the aircraft without surface discontinuities on the wing was sufficient.

Multiple diameters could have been used for calculating the ideal mass flow rate of the G-II engine. However, the CFD results demonstrated that while lowering the MFR value at the fan face caused more disruption in the region directly under the nacelle, the effects further outboard were relatively unchanged. All three MFR values used caused minimal effects after about 45 percent span. Therefore, as long as an MFR value that can be treated as a worst-case scenario was used in a CFD case, the engine effects could be effectively bracketed. By using the smaller diameter of the inlet for the ideal mass flow rate, the MFR of 0.5 represented such a scenario. Even at this extreme, the effects still dissipated sufficiently after 45 percent span.

Despite the effects of the engine on the wing's pressure field, the G-II was determined to be fully capable of serving as the test bed for the LFC flight experiments. At 45 percent and further outboard, the engine effects are accountable and a nearly spanwise-constant pressure distribution exists. This region could serve as an ideal location to mount a wing glove on the G-II. If the G-III is used instead, it should be an even more attractive candidate for the flight tests due to its larger chord. Proper wing glove placement on the G-III would be similar to the recommended location on the G-II.

While streamline deflection due to the fuselage played a large role in the O-2A flight experiments, it should not be a factor with this project. The application of DREs to control crossflow is dependent upon angle of attack. Since the SWIFT model was mounted vertically beneath the port wing of the O-2A, the streamline deflection from the fuselage in the spanwise direction correlated to a change in α for the SWIFT. Since the wing glove in this project is not mounted vertically but rather along the actual wing, this type of deflection only changes the β for the glove. As shown in the results, this change in β should only amount to about three degrees. The wing glove's α changes minimally due to deflection and should not have any significant effect on the experiment.

Based on the results of the G-II, smaller transport aircraft such as business jets with fuselage-mounted engines should experience pressure field distortions on the wing. Besides affecting the placement of a wing glove experiment, these effects make general laminar flow control in the affected region a difficult task. However, if the engine effects dissipate further outboard as seen in the G-II study, then laminar flow would be more easily realized in these regions. Further investigation into the pressure field distortion caused by the engines would be needed to determine the possibilities for achieving laminar flow on the wing of these types of aircraft.

The benefits of laminar flow for aircraft are well established. With such volatility in fuel prices and supply, laminar flow technology represents a valuable option for improving the efficiency of aircraft. Reducing the drag associated with an aircraft wing can provide numerous benefits to several different fields, ranging from the airline industry to military operations. With a successful demonstration of DRE technology on a swept-wing at eight million chord Reynolds number, laminar flow for transonic aircraft would be one step closer to being realized. The results from this study indicate that a successful demonstration of the DRE technology at chord Reynolds numbers between 15 and 20 million could be made possible by using one of these aircraft.

REFERENCES

[1] Bureau of Transportation Statistics, "Airline Fuel Cost and Consumption (U.S. Carriers – Scheduled)" [online database], http://www.transtats.bts.gov/fuel.asp [retrieved 13 February 2010].

[2] Green, J.E., "Laminar Flow Control – Back to the Future?," AIAA Paper 2008-3738, 2008.

[3] Reed, H.L., and Saric, W.S., "Transition Mechanisms for Transport Aircraft," AIAA Paper 2008-3743, 2008.

[4] Saric, W.S., Reed, H.L., and White, E.B., "Stability and Transition of Three-Dimensional Boundary Layers," *Annual Review of Fluid Mechanics*, Vol. 35, 2003, pp.413-40.

[5] Wassermann, P., and Kloker, M., "Mechanisms and Passive Control of Crossflow-Vortex-Induced Transition in a Three-Dimensional Boundary Layer," *Journal of Fluid Mechanics*, Vol. 456, 2002, pp. 49-84.

[6] Saric, W.S., and Reed, H.L., "Toward Practical Laminar Flow Control – Remaining Challenges," AIAA Paper 2004-2311, 2004.

[7] Wagner, R.D., and Maddalon, D.V., "Laminar Flow Control Leading-Edge Systems in Simulated Airline Service," *Journal of Aircraft*, Vol. 27, No. 3, 1990, pp. 239-244.

[8] Saric, W.S., and Reed, H.L., "Crossflow Instabilities – Theory and Technology," AIAA Paper 2003-771, 2003.

[9] Radeztsky, R.H., Reibert, M.S., and Saric, W.S., "Effect of Isolated Micron-Sized Roughness on Transition in Swept-Wing Flows," *AIAA Journal*, Vol. 37, No. 11, 1999, pp. 1370-1377.

[10] Saric, W.S., Carrillo, R.B., Jr., and Reibert, M.S., "Leading-Edge Rougness as a Transition Control Mechanism," AIAA Paper 1998-0781, 1998.

[11] Reibert, M.S., Saric, W.S., Carrillo, R.B., Jr., and Chapman, K.L., "Experiments in Nonlinear Saturation of Stationary Crossflow Vortices in a Swept-Wing Boundary Layer," AIAA Paper 1996-0184, 1996.

[12] Carpenter, A.L., Saric, W.S., and Reed, H.L., "In-Flight Receptivity Experiments on a 30-Degree Swept-Wing Using Micron-Sized Discrete Roughness Elements," AIAA Paper 2009-590, 2009.

[13] Gartenberg, E., and Roberts, A.S., Jr., "Twenty-Five Years of Aerodynamic Research with Infrared Imaging," *Journal of Aircraft*, Vol. 29, No. 2, 1992, pp. 161-171.

[14] Martin, M.L., Carpenter, A.L., and Saric, W.S., "Swept-Wing Laminar Flow Control Studies Using Cessna O-2A Test Aircraft, AIAA Paper 2008-1636, 2008.

[15] Rhodes, R.G., Carpenter, A.L., Reed, H.L., and Saric, W.S., "CFD Analysis of Flight-Test Configuration for LFC on Swept Wings," AIAA Paper 2008-7336, 2008.

[16] Jane's Aircraft Upgrades [online database], http://jau.janes.com.

[17] Direct Dimensions, Inc., "Almost Everything You Wanted to Know About 3D Scanning" [online], http://dirdim.com/lm_everything.htm [retrieved 20 February 2010].

[18] Aerospaceweb.org, "Atmospheric Properties Calculator" [online], Ver. 2.1.4, http://www.aerospaceweb.org/design/scripts/atmosphere, 2005.

[19] Rhodes, R.G., "Computations of Laminar Flow Control on Swept Wings as a Companion to Flight Test Research," Masters Thesis, Aerospace Engineering Department, Texas A&M University, College Station, TX, 2008.

[20] *FLUENT, Software Package*, Ver. 6.3.26, ANSYS Inc., Canonsburg, PA, 2010.

[21] *FLUENT, Software Package*, Ver. 12.0.16, ANSYS Inc., Canonsburg, PA, 2010.

[22] *GAMBIT, Software Package*, Ver. 2.3.16, ANSYS Inc., Canonsburg, PA, 2010.

[23] Agarwal, R., "Computational Fluid Dynamics of Whole-Body Aircraft," *Annual Review of Fluid Mechanics*, Vol. 31, 1999, pp. 125-69.

[24] Boppe, C.W., "Elements of Computational Engine-Airframe Integration," AIAA Paper 1984-0117, 1984.

[25] Flack, R.D., *Fundamentals of Jet Propulsion with Applications*, Cambridge University Press, New York, 2005.

[26] Mattingly, J.D., *Elements of Propulsion: Gas Turbines and Rockets*, AIAA Education Series, AIAA, Resont, VA, 2006.

[27] Chen, A.W., Curtin, M.M., Carlson, R.B., and Tinoco, E.N., "TRANAIR Applications to Engine/Airframe Integration," *Journal of Aircraft*, Vol. 27, No. 8, 1990, pp. 716-721.

[28] Uenishi, K., Pearson, M.S., Lehnig, T.R., and Leon, R.M., "Computational Fluid Dynamics Based Three-Dimensional Turbofan Inlet/Fan Cowl Analysis System," *Journal of Propulsion and Power*, Vol. 8, No. 1, 1992, pp. 175-183.

[29] Seddon, J., and Goldsmith, E.L., *Intake Aerodynamics*, 2nd ed., AIAA Education Series, AIAA, Reston, VA, 1999.

[30] Mund, F.C., Doulgeris, G., and Pilidis, P., "Enhanced Gas Turbine Performance Simulation Using CFD Modules in a 2D Representation of the Low-Pressure System for a High-Bypass Turbofan," *Journal of Engineering for Gas Turbines and Power*, Vol. 129, July 2007, pp. 761-768.

[31] Boppe, C.W., and Stern, M.A., "Simulated Transonic Flows for Aircraft with Nacelles, Pylons, and Winglets," AIAA Paper 1980-0130, 1980.

[32] Oberkampf, W.L., Sindir, M.M., and Conlisk, A.T., "Guide for the Verification and Validation of Computational Fluid Dynamics Simulations," AIAA Guide G-077-1998, 1998.

APPENDIX A

Below is a complete list of the aircraft examined as potential candidates for the flight tests.

Bombardier
Learjet 24
Learjet 25
Learjet 28
Learjet 29
Learjet 31
Learjet 35
Learjet 36
Learjet 45
Learjet 55
Learjet 60
Challenger 300
Challenger 600
Challenger 601
Challenger 604
Challenger 605
Challenger 800
Challenger 850
Global 5000
Global Express
Global Express XRS

British Aerospace
BAE 125

Cessna
510 Citation Mustang
525 CitationJet CJ1
525A CitationJet CJ2
525B CitationJet CJ3
525C CitationJet CJ4
550 Citation II
551 Citation II/SP
S550 Citation S/II

Cessna (cont.)
550 Citation Bravo
560 Citation V
560 Citation Ultra
560 Citation Encore
560 XL Citation Excel
560 XL Citation XLS
650 Citation III
650 Citation IV
650 Citation VI
650 Citation VII
680 Citation Sovereign
750 Citation X

Dassault
Falcon 10 and 100
Falcon 20 and 200
Falcon 50
Falcon 900
Falcon 2000
Falcon 7X

Douglas
X-21 (WB-66D)

Eclipse Aviation
Eclipse 500

Embraer
ERJ-135
ERJ-140
Legacy
ERJ-145

Gulfstream
Gulfstream II
Gulfstream III
Gulfstream IV, 300, 400
Gulfstream V, 500, 550
G100
G150
G200
G350, G450
G650

Hawker Beechcraft
Beechcraft Premier
Hawker 400
Hawker 750
Hawker 800
Hawker 850
Hawker 900
Hawker 1000
Hawker 4000

Lockheed
Jetstar

Sabreliner
Model 40
Model 60
Model 65
Model 75
Model 80

APPENDIX B

The following is a specific journal file used for setting up the boundary conditions in FLUENT. It can be tailored for different boundary types, different boundary names, and different boundary conditions.

```
;The following automates various boundary and operating specifications
;for the CFD case setup in FLUENT. The boundary names must match those
;specified in GAMBIT.

/define/operating-conditions/operating-pressure
0      ;Operating static pressure

/define/boundary-conditions
pressure-far-field
front       ;Boundary name
no
393.12      ;Static pressure
no
0.75      ;Mach no.
no
390       ;Static temperature
yes
no
-1      ;x-direction flow
no
0       ;y-direction flow
no
0       ;z-direction flow

;These are the domain boundaries (5).
/define/boundary-conditions
pressure-far-field
back
no
393.12
no
0.75
no
390
yes
no
-1
no
0
no
0

/define/boundary-conditions
pressure-far-field
```

```
port
no
393.12
no
0.75
no
390
yes
no
-1
no
0
no
0

/define/boundary-conditions
pressure-far-field
top
no
393.12
no
0.75
no
390
yes
no
-1
no
0
no
0

/define/boundary-conditions
pressure-far-field
bottom
no
393.12
no
0.75
no
390
yes
no
-1
no
0
no
0

;This is the fan face boundary.
/define/boundary-conditions
pressure-outlet
engine_fan_face
no
```

```
470       ;Static pressure
no
430       ;Static temperature
no
yes
no
yes
no
32.8      ;Target mass flow rate
no
104427.74   ;Upper pressure bound (default value)
no
0.020885547    ;Lower pressure bound (default value)

;This is the exhaust face boundary.
/define/boundary-conditions
mass-flow-inlet
engine_exhaust
yes
yes
no
54.0      ;Mass flow rate
no
1080      ;Total temperature
no
420       ;Static pressure (only for supersonic)
yes
yes
no
-1        ;x-direction flow
no
0         ;y-direction flow
no
0         ;z-direction flow
```

APPENDIX C

The following figures show the streamlines over the G-II wing. The streamlines are colored by static pressure values.

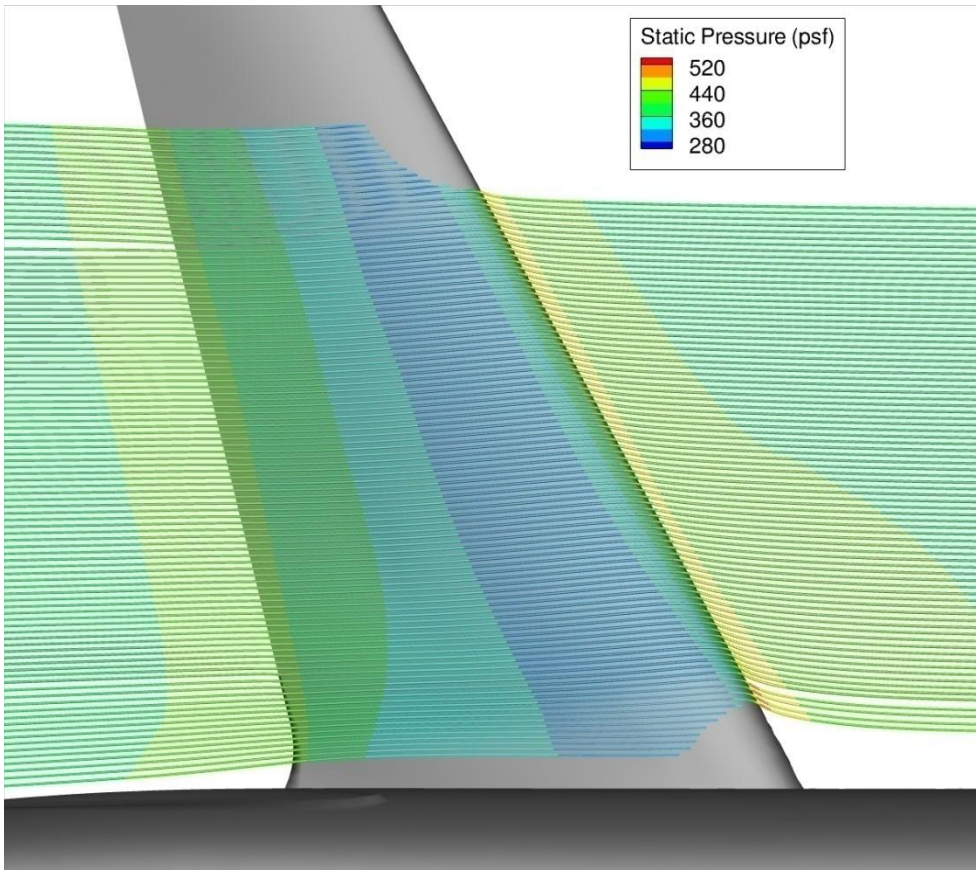

Fig. C1 Streamlines over wing for no-nacelle model.

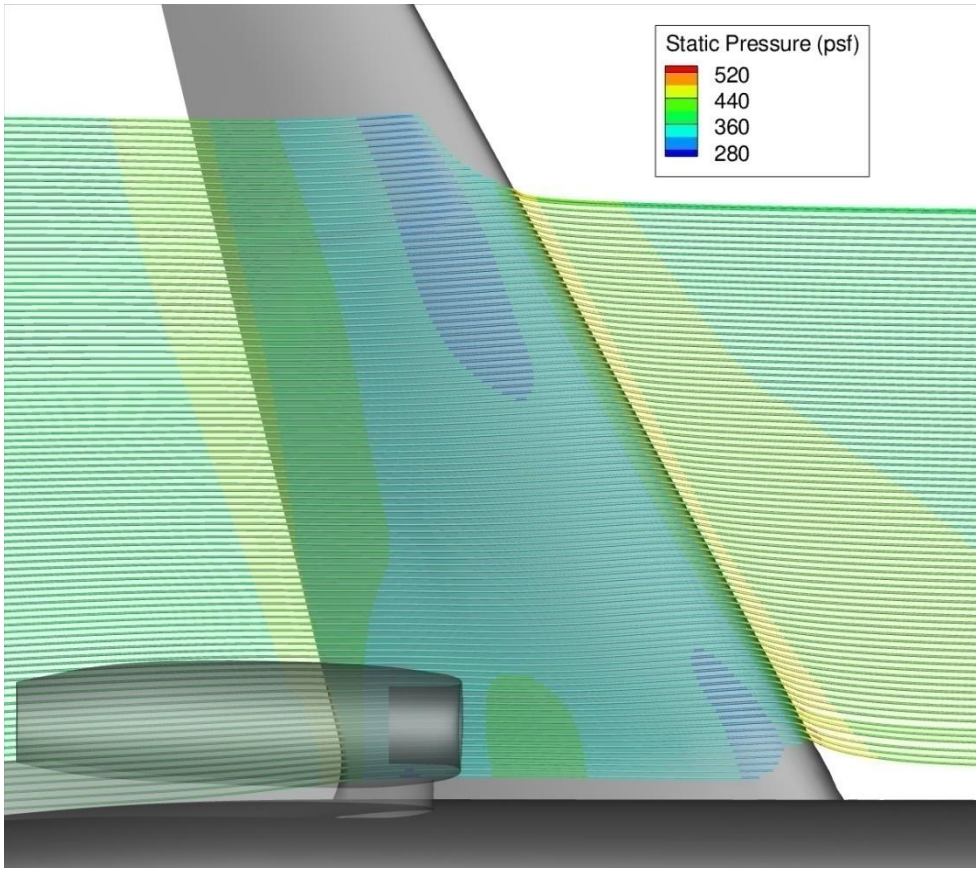

Fig. C2 Streamlines over wing for 0.5 MFR. No differences in streamline direction are noticeable when compared to the no-nacelle results.

VITA

Name:	Tyler Patrick Neale
Address:	Texas A&M University Department of Aerospace Engineering H.R. Bright Building, Room 701, Ross Street – TAMU 3141 College Station, TX 77843-3141
Email Address:	tpneale@gmail.com
Education:	B.S., Mechanical Engineering, Louisiana Tech University, 2008 M.S., Aerospace Engineering, Texas A&M University, 2010